Dipartimento di Fisica e Astronomia Galileo Galilei
Università degli studi di Padova

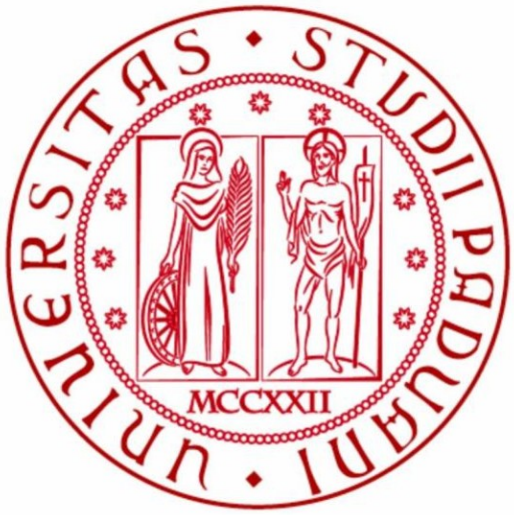

Study of the internal cavity and of the spiral arms in the system HD100453 through hydrodynamical simulations

Delibori Enrico

Relatori:

Francesco Marzari
Cornelis P. Dullemond

Correlatore:

Giovanni Carraro

Abstract

In the last 25 years, extrasolar planets detection and study has become one of the most important topics in modern astrophysics. Since in a lot of cases their direct detection is quite difficult or impossible with the actual instruments, other methods have been developed to find and/or characterize them, in order to study the diversities and the population of planets and planetary systems around stars.
Such methods include also the study of large-scale structures that appear in several disks. It is possible to see them through very high resolution observations, in particular thanks to ALMA, or SPHERE. Some of these structures, such as cavities, gaps or rings can be proofs of perturbations generated by massive companions that modify their surrounding environment. These are typical in the so-called *transition disks*, old disks that are *transiting* from a pure gas structure to a planetary system, more similar to the Solar one.
Other type of structures, such as spiral arms or shadows, were detected in various disks, but not only planets were suggested as candidates for their formation: shadows can be due to inner disk misalignments; rings can be a consequence of stellar outbursts; spiral arms can be related to shadows in disk or to the presence of external (eventually unseen) massive companions.
In this thesis work the specific system HD100453 is taken in consideration. From its high resolution observations it's possible to notice several structures inside it: a cavity, spiral arms and shadows.
The main purpose of this work is an attempt in reproducing some of the observed structures through hydrodynamical simulations via the FARGO3D code (Benítez-Llambay and Masset, 2016).
In this system a M-dwarf star (HD100453 B) has been detected at a distance of 120 AU from the main object and external to the disk. It was considered as the main responsible for the triggering and development of the observed spiral arms. This star also causes a tidal truncation of the disk, reducing its radius to a maximum of $\sim 40 - 45$ AU, much lower than typical dimension of a protoplanetary disk. Also will be analyzed the differences when the companion star has an eccentric orbit.
Moreover, the presence of an internal planet, still not detected and presumably located between at about 10 AU from the main star, is considered as a candidate responsible for the creation of the inner cavity observed in the disk. So a second set of simulations with two companions has been performed, trying to characterize the planet that could generate the inner hole, and also checking its effects on the spiral arms.
The images derived from observations are scattered-light images tracing the dust on the *surface* layers of the disk. The simulations are performed only in a 2-dimensional

frame, and they just trace the gas behavior due to the gravitational perturbations generated by the companion(s). They trace the integrated density along the disk height, not just its surface. This must be taken in consideration in the calculation of the truncation radius, of the pitch angle of the spiral arms, and of the cavity wideness.

This thesis work is organized as follows: Chapter 1 describes the typical structure and evolution of a protoplanetary disk; in Chapter 2 there is the description of the system that has been studied, HD100453; in Chapter 3, the FARGO3D code is briefly described, and the simulation setups are explained; Chapter 4 shows the results obtained through the simulations; Chapter 5 includes final considerations and future improvements.

Astratto

Negli ultimi 25 anni, la ricerca e lo studio di pianeti extrasolari sono diventati oggetto di grande interesse nell'ambito dell'astrofisica moderna. Poichè però la loro rilevazione non è banale, se non impossibile con la strumentazione attuale, altri metodi sono stati sviluppati per poterli identificare e/o caratterizzare, allo scopo di studiare la loro diversità e le popolazioni di pianeti o sistemi planetari attorno ad altre stelle.
Tra questi metodi vi è lo studio di strutture su larga scala che appaiono in svariati dischi. Queste sono visibili tramite osservazioni ad elevata risoluzione angolare, effettuate tramite ALMA o SPHERE. Alcune tra queste strutture, tra le quali cavità, spazi vuoti o anelli, sembrano essere dovuti a perturbazioni generate da corpi massicci, come dei pianeti, che modificano il proprio ambiente circostante. Questi ultimi sembrano piuttosto comuni nei cosiddetti *dischi di transizione*, dischi in stadio avanzato che stanno *transitando* da una struttura quasi interamente fatta di gas a un sistema planetario vero e proprio, simile al sistema Solare.
Anche altri tipi di strutture sono state rilevate, come bracci di spirale o zone in ombra, ma non sempre la causa della loro presenza sembra essere un pianeta: per esempio certe zone del disco principale di un sistema possono essere messe in ombra da una componente più piccola disallineata col resto del sistema, e più vicina alla stella; gli anelli possono essere dovuti a episodi collegati all'evoluzione della stella, come dei brillamenti; i bracci di spirale possono essere innescati dalle zone in ombra, o dalla presenza di una componente binaria esterna al sistema, spesso non rilevata o risolta.
In questo elaborato di tesi l'oggetto di studio è il sistema HD100453. Da osservazioni ad alta risoluzione è stato possibile rilevare diverse strutture nel disco del sistema, tra cui una cavità centrale, dei bracci di spirale e delle zone in ombra.
L'obiettivo principale è la riproduzione di alcune di queste strutture tramite simulazioni numeriche di idrodinamica effettuate attraverso il codice FARGO3D (Benítez-Llambay and Masset, 2016).
In questo sistema è stata rilevata una stella compagna (HD100453 B) che orbita attorno alla stella principale ad una distanza di 120 AU, esternamente al disco protoplanetario. Questa stella viene considerata la principale responsabile della formazione e del mantenimento della struttura a spirale osservata. Sembra inoltre essere la causa del troncamento del disco, riducendone il raggio a $\sim 40 - 45$ AU, un valore molto inferiore alla dimensione tipica di un disco protoplanetario. Nelle simulazioni verranno inoltre analizzate le differenze a seconda che l'orbita della compagna sia circolare o ellittica.
Successivamente un secondo corpo viene inserito nelle simulazioni: esso è un pianeta

a una distanza di ~ 10 AU, attualmente non rilevato. La sua presenza sarebbe all'origine dell'apertura della cavità osservata. Un secondo set di simulazioni è dedicato alla caratterizzazione di tale pianeta, facendo anche attenzione a come questo possa modificare la struttura a spirale.
Le immagini che derivano dalle osservazioni rilevano la luce deviata dalle particelle di polvere che si trovano sulla *superficie* del disco. Le simulazioni sono bidimensionali, e considerano solo il moto del gas causato dalle perturbazioni gravitazionali dei corpi. Esse forniscono l'evoluzione della densità del gas integrata lungo la coordinata verticale del disco, e non ne tracciano propriamente l'evoluzione in superficie. Questo è un fattore da tenere in considerazione nel calcolo del raggio a cui il disco viene troncato, dell'angolo di apertura dei bracci di spirale e dell'ampiezza della cavità centrale.

Il seguente elaborato è suddiviso come segue: il Capitolo 1 consiste in una panoramica sulla struttura fisica dei dischi protoplanetari; il Capitolo 2 descrive il sistema considerato, HD100453; nel Capitolo 3 vi è un'introduzione al funzionamento del codice utilizzato, FARGO3D, e vengono spiegati i setup utilizzati per le simulazioni; nel Capitolo 4 vengono mostrati e analizzati i risultati di tali simulazioni; il Capitolo 5 contiene una rassegna dei riusltati ottenuti e di possibili sviluppi futuri.

Contents

Chapter 1

Protoplanetary disks

Around newly born stars (protostars) are usually present disks of gas and dust that can extend until several hundreds of AU from the main object: these structures are identified as **protoplanetary disks**, and are supposed to be the place where planetary systems form.
Their presence was predicted from star formation theories and models (Shakura and Sunyaev, 1973), and later confirmed by observations.

1.1 Observations

The observation of protoplanetary disks isn't trivial because of different reasons. First of all, they are present only around very young stars, since their lifetime is really short with respect to main sequence stars.
Their distance is often a problem because of the limited resolution: a system at about 100 pc far from us has an angular dimension of the order of 1", or even less if enough small.
The majority of disks have been revealed thanks too infrared (IR) observations of very young stars, with the InfraRed Astronomical Satellite (IRAS). Looking at their Spectral Energy Distribution (SED), these sources exceed in their IR emission in comparison to a simple black-body spectrum (Figure 1.1). This excess is due to the presence of dust around the star, that absorbs the UV and the optical emission from the star and re-emits in the IR. This dust is a remnant of the molecular cloud from which the system took its origin (Section 1.2). Looking at the continuum radiation that it generates it's possible to map the temperature along the radial direction and to estimate the disk mass.
Thanks to some telescopes like *Hubble*, ALMA or SPHERE it is possible to resolve some disks. It was discovered that several protoplanetary disks show large scale structures, such as rings, cavities, gaps, shadows, spirals, or some other type of azimuthal asymmetries. These can be generated by a bunch of physical processes; for example, they can be consequences of vortexes or planets formation. Planets (or massive companions) can be really difficult to identify through direct imaging, because of the high contrast with the star that hosts them. So the study of these

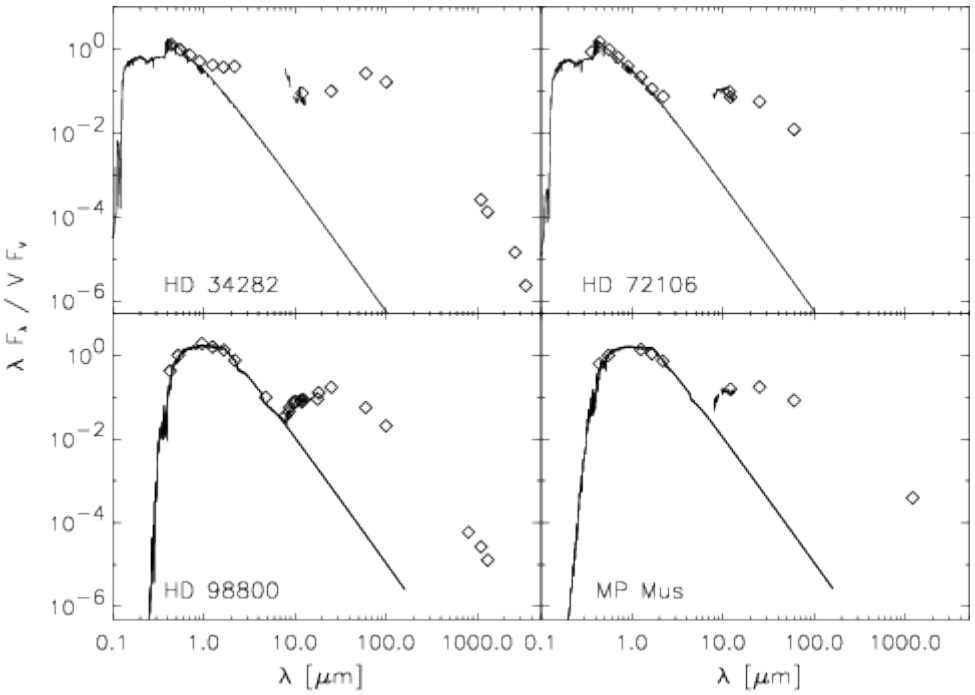

Figure 1.1: Example of IR excess due to the protoplanetary disks emission (*dots*). The *solid line* represents the black-body spectrum of the central star, which doesn't match the IR data. Image from Schütz et al. (2005).

structures offers an alternative way to identify and characterize them, and can help the understanding of their formation (for example through dust traps).

1.2 Disk formation and lifetime

The most accepted theories nowadays establish that a protoplanetary disk forms together with a star during the gravitational collapse of a molecular cloud. These last ones are approximately spherical ramming of gas and dust in the interstellar medium, with radius R_{cl} of the order of 10 pc, masses M_{cl} of about $10^5 M_\odot$, and are characterized by very low densities ($\rho \sim 10 - 100\, particles/cm^3$) and temperatures ($T \simeq 10 - 100$ K).
If a perturbation involves enough material, the pressure forces of the gas, that tends to expand its volume, are no more able to balance the gravitational ones. As a consequence, the cloud (or part of it) tends to collapse. The material involved must have a mass bigger than the so called *Jeans mass* to start the collapse. This is derivable from the hydrostatic equilibrium condition

$$\frac{GM_{cl}}{R_{cl}} = \frac{k_B T}{\mu\, m_H} \tag{1.1}$$

where G is the gravitational mass, k_B the Boltzmann constant, μ the mean molecular weight, assumed to be equal to 2.4 in a typical molecular cloud, and m_H the hydrogen mass. When the left term overcome the right one, the gravitational forces drive the

collapse of the cloud. For the typical values of R_{cl} and T this happens when

$$M_{cl} \geq M_J \simeq 4 \cdot 10^4 \left(\frac{T}{100\,K}\right)^{3/2} \left(\frac{n}{cm^3}\right)^{-1/2} \tag{1.2}$$

which is typically about $10^3 - 10^4 M_\odot$ (n is the number density of the particles in the cloud). At this point the involved part of the cloud collapses with a dynamical timescale $\tau_{dyn} \propto \rho^{-1/2}$, in an isothermal way until it is no more transparent to IR light. When it gets opaque to this, the material heats up and returns able to contrast the gravity, reaching a quasi-static equilibrium condition. The bulk of material that forms at the center of this region is called **protostar**.
Since a symmetrically spherical collapse is impossible to verify, the cloud necessarily will rotate around a certain axes. Thanks to the conservation of the angular momentum, the material that still doesn't accrete the protostar starts to settle on the equatorial plane of the system, perpendicular to the rotation axes. This material will constitute a tiny disk structure that will rotate around the bulk of the collapsed cloud, and will form the **protoplanetary disk** associated to the (proto)star. This structure is considered the birthplace of **planetary systems**. The disposition of the planets of the Solar system seems to confirm this theory, since they are approximately almost all on the elliptical plane.

Typically, this disk structure forms in about $10^4 - 10^5$ years from the collapse and has a lifetime between 10^6 and 10^7 years. This can be inferred from the observations of the IR light processed by the dust in the disk, if the age of the main star is known through other ways. Planetary systems must form during this period time, which is very short in comparison to the one of a solar-like star of $10^9 - 10^10$ years.
Moreover, the disk lifetime can be seriously influenced by different factors, both external (like the presence of UV radiation, for example from near O-B stars) and internal to the system. The HD100453 system, that will be studied later, presents a secondary dwarf star (see Chapter 2 for more details) that causes the truncation of the disk, drastically reducing the lifetime of its external zone to a few dynamical timescales (Section 1.6).

1.3 Disk models

For the study of the evolution of protoplanetary disks, it is necessary to have some physical models that can describe their mechanical and thermal structure.
Given the shape of a disk, the most intuitive coordinate system that will be adopted to describe it will be the *cylindrical* one, characterized by the radial, the azimuthal and the vertical coordinates (r, φ, z).

1.3.1 Vertical structure

Let's consider an optically thick disk, heated by the stellar radiation, and with mass $M_{disk} \ll M_*$ to avoid self-gravitating effects. With these conditions, and considering

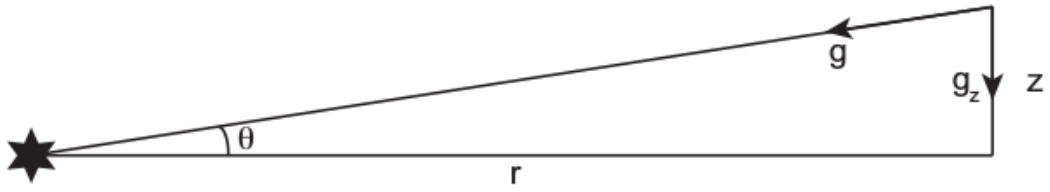

Figure 1.2: Geometry for the calculation of $\rho(z)$.

azimuthal symmetry, consider a particle in a position $(r,\ z)$. Along the vertical direction, this will be in a condition of hydrostatic equilibrium if

$$\frac{dP}{dz} = -\rho\, g_z = -\frac{GM_*}{r^2+z^2}\rho\sin(\theta) \simeq -\frac{GM_*}{r^2+z^2}\,\rho\,\frac{z}{(r^2+z^2)^{1/2}} \simeq -\rho\,\frac{GM_* z}{r^3} \tag{1.3}$$

where P is the pressure, ρ is the density of the disk, M_* the mass of the central star (considered as the only source of gravitational forces), and θ the angle from the midplane (see Figure 1.2). The last identity is valid since $z \ll r$ in a typical disk. Since the **keplerian velocity** is defined as $\Omega_K = \sqrt{GM_*/r^3}$, the previous equation can be written as

$$\frac{1}{\rho}\frac{dP}{dz} = -\Omega_K^2\, z \tag{1.4}$$

Assuming the gas as perfect, the pressure can be written as $P = \rho c_s^2$, with $c_s = \sqrt{k_B T/(\mu\, m_H)}$ the *sound speed*, such as

$$c_s^2\,\frac{d\rho}{\rho} = -\Omega_K^2\, z\, dz \tag{1.5}$$

if the pressure changes negligibly along the vertical coordinate. The solution of this equation leads to the following expression for the density:

$$\rho(z) = \rho_0 \exp\left(-\frac{z^2}{2H^2}\right) \tag{1.6}$$

where ρ_0 is the density at the midplane and $H = c_s/\Omega_K$ is the *vertical disk height*. This last quantity is depending on the disk temperature through c_s, and on the radius through Ω_K. Dividing it by the radius it's possible to obtain the *aspect ratio* $h = H/r = c_s/(\Omega_K r) = c_s/v_K$.
The density ρ is related to another useful quantity, the **surface density** $\Sigma = \int_{-\infty}^{+\infty} \rho\, dz$. Through this quantity, it is possible to express the constant ρ_0, such that the Equation 1.6 becomes

$$\rho(z) = \frac{\Sigma}{\sqrt{2\pi}\, H} \exp\left(-\frac{z^2}{2H^2}\right) \tag{1.7}$$

1.3.2 Radial structure

Regarding the *radial structure* of the disk, it is necessary to find an expression for $\Sigma(r)$, assuming an azimuthally symmetric disk. This typically assumes a power-law

form, with index p, multiplied by an exponential cut-off, with R_C the cut-off radius:

$$\Sigma(r) = \Sigma_0 \left(\frac{r}{R_0}\right)^{-p} \exp\left(-\frac{r}{R_C}\right) \tag{1.8}$$

where R_0 is just a reference value of the radius, and $\Sigma_0 = \Sigma(R_0)$ is the surface density value at that point. The value of p can be inferred from observation and models. A first one was found through the analysis of the *minimum mass Solar nebula* (Hayashi, 1981; Weidenschilling, 1977), which is the minimum mass that should characterize the primordial disk of the Solar system in order to form the actual bodies. This lead to a surface density distribution of the gas component of $\Sigma(r) = 1.7 \cdot 10^3\, r^{-3/2}$ (with $R_0 = 1$ AU), so $p = 3/2$. But the Solar system isn't representative of all the other planetary systems; through some observations other models were proposed and found values of $p = 1$ (Andrews et al., 2009).
The cut-off is imposed because, since usually $p < 2$, the mass of the disk $M_{disk} \propto r^2\Sigma$ would rise to infinite without it. Moreover, since the initial collapsing cloud has a finite size, even the formed disk can't extend to infinite. Typical values of R_C can go from several tens to some hundreds of AU (Hughes et al., 2008).
This value can be inferred through observations, and it is strictly related to the maximum radius of the disk R_{out}, that can span from less than 100 AU to about 1000 AU.
On the other hand, it is also necessary to establish the minimum radius of the disk R_{in}, since in the inner zones the material can be dissipated by the stellar radiation. This value depends on the specific disk and on the type of the central star, and can vary from ~ 0.1 to ~ 10 AU. It is typically inferred from SEDs shape.

1.3.3 Viscosity

The radial velocity of the material in the disk is $v_r \ll v_\varphi$, so the gas motion in the radial direction seems to be negligible. But since star accretion is often observed, there must be at least a mechanism that triggers the transport of the angular momentum of the gas. This must be related to the presence of a **cinematic viscosity** ν in the equation of the temporal evolution of the surface density, and in general in the hydrodynamical equations of the gas (see Section 3.1).
However, the processes involved in its determination are still not completely understood: this viscosity can't be simply associated to the *molecular viscosity*, since such a consideration would drive the gas inward in a very long time, inconsistent with disk lifetimes (Pringle, 1981). As a consequence, the angular momentum transport must be driven by some kind of turbulences, which origins are still not well determined. Several mechanisms that can verify (or are favored) in certain physical conditions are:

- Magneto-Rotational Instabilities (MRI), that can play a significant role in sufficiently high ionized disks (Balbus, 2003).
- Gravitational instabilities, that can arise when the disk is enough massive ($M_{disk} \geq 0.1\, M_*$) (Toomre, 1964).

- Baroclinic instabilities and vertical shear instabilities, that can appear when the radial temperature (Stoll and Kley, 2014) or entropy gradient (Klahr and Bodenheimer, 2003) that characterize the disk are too steep.
- Others that involve also the solid part of the disk, like induced Kelvin-Helmholtz instabilities and streaming instabilities.

Usually it's difficult to determine whether one between these effects can be dominant on the others. A classical way to summarize the viscosity of the turbulences that all these processes can generate inside the disk is the so-called *α-prescription* by Shakura and Sunyaev (1973). In this approach, the gas is supposed to move through the disk in *eddies*. These shall have a dimension lower than the disk height H, and shall move inward with a velocity lower than c_s, otherwise the turbulence would break. With these considerations it is possible to express the cinematic viscosity as

$$\nu = \alpha\, c_s\, H \tag{1.9}$$

Here α is a dimensionless quantity that typically assumes values from 10^{-5} to 10^{-2}, depending on the specific disk. It is a parameter used to shift on itself all the uncertainties regarding the generation of ν. It smoothly changes with temperature and radius, and it is often implemented in hydrodynamical simulation codes.

The viscosity enters in several equations regarding the structure and the evolution of a protoplanetary disk. For example the one for the evolution of surface density contains it[1]

$$\frac{\partial \Sigma}{\partial t} = \frac{3}{r}\frac{\partial}{\partial r}\left[r^{1/2}\frac{\partial}{\partial r}\left(\nu\,\Sigma\, r^{1/2}\right)\right] \tag{1.10}$$

Other mechanisms have been proposed to explain the transport of the angular momentum: these involve non-ideal magnetohydrodynamical effects, such as ambipolar diffusion or the Hall effect (Turner et al., 2014).

1.3.4 Velocities

Let's see now the relation between the speed sound c_s, the keplerian velocity v_K and the effective azimuthal velocity v_φ. The first is proportional to $\sqrt{T}$, and since from observations results $H \simeq 0.1\, r$, so $c_s \simeq 0.1\, \Omega_K$.
Considering a quasi-stationary disk ($\partial\vec{v}/\partial t = 0$) it's possible to calculate v_φ through the momentum equation along the azimuthal coordinate:

$$\frac{v_\varphi^2}{r} = \frac{GM_*}{r^2} + \frac{1}{\rho}\frac{dP}{dr} \tag{1.11}$$

Since the gas pressure decreases while going outward ($dP/dr < 0$)[2], this implies $v_\varphi < v_K$. Let's roughly estimate their difference:

$$\frac{1}{\rho}\frac{dP}{dr} \simeq \frac{1}{\rho}\frac{\rho c_s^2}{r} = \frac{c_s^2}{r} = \frac{\Omega_K^2 H^2}{r} \tag{1.12}$$

[1] This is valid if the angular velocity is assumed to be Keplerian, $\Omega \propto r^{-3/2}$

[2] This approach doesn't apply to dust particle, the pressure acts only on the gas!

such that

$$v_\varphi = \Omega_K r \left(1 - \frac{H^2}{r^2}\right) = v_K \left(1 - \frac{H^2}{r^2}\right) \tag{1.13}$$

This means that the azimuthal velocity can be considered equal to the keplerian one, since for a typical disk $H \ll r$. Moreover, since the values of v_K can reach values higher than 10^3 km/s, it's clear that $v_\varphi \simeq v_K \gg c_s$. This means that protoplanetary disks are nearly keplerian disks.
Regarding the radial velocity v_r of the gas, this can be expressed in function of the viscosity as[3]

$$v_r \simeq \frac{3}{2}\frac{\nu}{r} = \frac{3}{2}\frac{\alpha c_s H}{r} \tag{1.14}$$

Since typically $H/r \ll 1$ and $\alpha < 1$, it follows that $v_r \ll c_s$. Inserting typical values for its calculation, it's easy to see that also $v_r \ll v_\varphi$.

1.3.5 Mass accretion

Even if the radial velocity is small, it is different from 0, and this leads the gas to move inward in the disk and to accrete the mass of the central star. The *mass accretion rate* can be expressed as follows:

$$\dot{M} = 2\pi r \, \Sigma \, v_r = 3\pi \, \Sigma \, \nu \tag{1.15}$$

For a steady-state accretion disk, the value of $\dot{M}$ results to be constant. For typical values of Σ and v_r, the values for $\dot{M}$ are of about $10^{-8} \, M_\odot/yr$, in agreement with the ones found through the observations (Manara et al., 2016).

1.3.6 Temperature

1D model

Let's have a look at the thermal physics of a protoplanetary disk. At first, consider a 1-dimensional model along the radial direction (assuming azimuthal symmetry): a first approximative temperature profile is a power-law

$$T(r) = T_0 \left(\frac{r}{R_0}\right)^{-q} \tag{1.16}$$

where R_0 and $T_0 = T(R_0)$ are reference values, as in the surface density equation (1.8). Typical values of q for classical disk structure models are inferred from the relation $p + q = 3/2$. This can be derived considering the profiles for $\Sigma(r)$ and $T(r)$ (Eq. 1.8 and 1.16), and that

$$\nu \propto c_s H \propto \frac{c_s^2}{\Omega_K} \propto \frac{T}{r^{-3/2}} \tag{1.17}$$

Inserting this in the equation 1.15:

$$\dot{M} \propto \frac{r^{-p} \, r^{-q}}{r^{-3/2}} \propto r^{-(p+q-3/2)} = const. \tag{1.18}$$

[3] It is assumed to have a steady-state accretion disk.

from which results the previous relation.

To determine the **effective temperature** of a protoplanetary disk, it's necessary to consider which are the *heating* and *cooling* mechanisms that happen inside it.

- One of the heating mechanisms is the **viscous heating** due to the accretion process: the heating per gram q_+ of the gas is proportional to its viscosity ν, and to the square of the shear. Multiplying this quantity for the surface density Σ it's possible to obtain the total heating per surface unit:

$$Q_+^{accr} = \Sigma\,\nu \left(r \frac{d\Omega_K}{dr} \right)^2 = \frac{9}{4}\,\Sigma\,\nu\,\Omega_K^2 = \frac{3}{4\pi}\dot{M}\,\Omega_K^2 \tag{1.19}$$

  where the expression for Q_+^{accr} has been combined with the one for the mass accretion (Eq. 1.15). Since this is constant, and the keplerian velocity is proportional to $r^{-3/2}$, this means that $Q_+^{accr} \propto r^{-3}$.

- Another heating process is due to the **irradiation** from the central star. Since disks are typically optically thick, this process will act only on its surface layers, and so it will depend on the *geometry* of the disk. This is related to the trend of the aspect ratio with the radius, so it depends on the value of β in the relation $H/r \propto r^\beta$. If $\beta > 0$, the disk is said to be *flared*, if $\beta = 0$ it's *flat*, if $\beta < 0$ is *self-shadowed*. In this last case, the surface areas closer to the star are the only ones directly irradiated by the central star; but under typical assumptions, most disks appear to be flared. Since $H \ll r$, the angle θ under which the surface is irradiated is very small. So, given a stellar flux

$$F_* = \frac{L_*}{4\pi r^2} \tag{1.20}$$

  where L_* is the star luminosity, the flux that irradiates the disk will be

$$F^{irr} = F_* \sin(\theta) \simeq \frac{L_*}{4\pi r^2}\,\theta \tag{1.21}$$

  The irradiation heating of the disk is twice this quantity, since both of its sides must be considered. So, the expression for it is

$$Q_+^{irr} = \frac{L_*}{2\pi r^2}\,\theta \tag{1.22}$$

- To avoid a continuous arise in the disk temperature, some cooling process needs to verify inside it. As an approximation, let's consider the disk surface radiation as a Planck function: the cooling rate, considering the two sides, will be

$$Q_- = 2\sigma_{SB} T_{eff}^4 \tag{1.23}$$

  where σ_{SB} is the Stefan-Boltzmann constant and T_{eff} the effective temperature.

Equating the heating and the cooling rate, such as $Q_- = Q_+^{accr} + Q_+^{irr}$, it is possible to find the expression for T_{eff}:

$$T_{eff} = \left(\frac{3\dot{M}\,\Omega_K^2}{8\pi\,\sigma_{SB}} + \frac{L_*\,\theta}{4\pi r^2\,\sigma_{SB}} \right)^{1/4} \tag{1.24}$$

The first term on the right side, due to accretion, prevails at inner radii; in such a case

$$T_{eff} \propto \dot{M}^{1/4}\, r^{-3/4} \tag{1.25}$$

When instead the irradiation term is the most important (typically at larger radii), the temperature profile follows the trend

$$T_{eff} \propto L_*^{1/4}\, r^{-1/2} \tag{1.26}$$

These laws establish the value of q in the Equation 1.16.

2D model

Until now the temperature along the vertical coordinate has been considered constant, such as $\partial T/\partial z = 0$. To expand the previous model along the z coordinate, it is necessary to have a deeper knowledge of the material properties.
First of all, dust assumes a very important role. Its mass percentage with respect to the gas is established through the *dust-to-gas ratio* η, which assumes values around 0.01 for typical disks. Even if this factor is very low, the **dust opacity** dominates on the gas one in determining the thermal structure. But this is very dependent on the frequency of the radiation, and on dust composition and size. Let κ_d be the mean dust opacity in the IR. This leads to the following expression for the optical depth at these wavelengths:

$$\tau_d = \frac{1}{2}\Sigma\,\eta\,\kappa_d \tag{1.27}$$

where Σ is referred to the gas distribution, not to the dust one.
As for the 1D model, let's consider the two heating mechanisms separately.

- For the **viscous** heating, let T_{eff} be the temperature at the surface height H_S. To find the temperature at $z < H_S$ it's necessary to use radiative diffusion theory; in high optical depth conditions ($\tau_d \gg 1$), the bolometric radiative flux is

  $$F(z) = -\frac{4\sigma_{SB}}{3\rho\eta\kappa_d}\frac{dT^4(z)}{dz} \tag{1.28}$$

  Assuming for simplicity that all the viscous heating is released at the midplane ($z = 0$), half of it will be directed to the upper part of the disk and half to the bottom one. This means that, for one side

  $$F(z) = \frac{1}{2}\,Q_+^{accr} \tag{1.29}$$

  Inserting this in Eq. 1.28:

  $$\frac{dT^4(z)}{dz} = -\frac{3\rho\eta\kappa_d}{8\sigma_{SB}}\,Q_+^{accr} \tag{1.30}$$

Integrating this from $z = 0$ to $z = H_S$ it's possible to obtain an expression for the temperature at midplane T_{mid} as a function of the effective temperature on the disk surface:

$$\int_0^{H_S} \frac{dT^4(z)}{dz}\, dz = -\frac{3\eta\kappa_d}{8\sigma_{SB}}\, Q_+^{accr} \int_0^{H_S} \rho\, dz \tag{1.31}$$

Assuming that $H_S \gg H$ (the disk height), so that most of the mass lies under the disk surface, the previous expression can be written as

$$T_{mid}^4 - T_{eff}^4 \simeq \frac{3\eta\kappa_d}{8\sigma_{SB}}\, Q_+^{accr} \int_0^{\infty} \rho\, dz = \frac{3\eta\kappa_d}{16\sigma_{SB}} \Sigma\, Q_+^{accr} = \frac{3\tau_d}{8\sigma_{SB}}\, Q_+^{accr} \tag{1.32}$$

since by definition $\Sigma = \int_{-\infty}^{+\infty} \rho\, dz$.
If only this heating term is considered, the cooling rate will equal it, such as $Q_+^{accr} = Q_- = 2\sigma_{SB} T_{eff}^4$. Substituting it in the previous equation, a final expression is obtained for T_{mid} as a function of T_{eff}:

$$T_{mid} = T_{eff} \left(\frac{3}{4}\,\tau_d + 1\right)^{1/4} \simeq T_{eff} \left(\frac{3}{4}\,\tau_d\right)^{1/4} \tag{1.33}$$

since $\tau_d \gg 1$ in the interior disk.

- Let's consider now the irradiation heating process, assuming the disk to be *flared*. A dust particle above the disk photosphere will entirely receive the stellar flux: if a is the radius of the dust particle, which is assumed to be spherical, the power it absorbs will be equal to $\pi a^2 F_*\ erg/s$. This must equal the one thermally emitted, which is $4\pi a^2 \sigma_{SB} T_d^4\ erg/s$. Equating the two, the expression for the temperature of dust at $z > H_S$ is

$$T_S = \left(\frac{\kappa_*}{\kappa_d} \frac{F_*}{4\sigma_{SB}}\right)^{1/4} = \left(\frac{\kappa_*}{\kappa_d} \frac{L_*}{16\pi r^2 \sigma_{SB}}\right)^{1/4} \tag{1.34}$$

where the factor κ_*/κ_d has been added to consider an eventual different dust opacity in the optical wavelengths, which average is κ_*. This ratio is closer to 1 when the dust size is bigger.
Even if $T_S \propto r^{-1/2}$, typically it is inferred from observations that $T_S > T_{eff}$, which has the same radius dependence. In a simplified model, the temperature for the dust at the surface is calculated using a damped expression for the stellar flux received: the flux F_* becomes $F_* \exp(-\tau_*)$, where τ_* is the optical depth at optical wavelengths. So the dust temperature at the surface becomes

$$T_S = \left[\exp(-\tau_*)\, \frac{\kappa_*}{\kappa_d} \frac{L_*}{16\pi r^2 \sigma_{SB}}\right]^{1/4} \tag{1.35}$$

This is valid until $T_S > T_{eff}$ for the irradiation heating model expressed in Eq. 1.24 (second term in the parenthesis). In general it's possible to express the dust temperature due to stellar irradiation as

$$T_{irr} = [T_S^4 + T_{eff}^4]^{1/4} \tag{1.36}$$

Finally, considering both viscous and irradiation heating, it's possible to have a final estimation of the vertical temperature structure as

$$T(z) = [T_{accr}^4(z) + T_{irr}^4(z)]^{1/4} \tag{1.37}$$

1.4 Transition disks

After some Myr from their formation, the inner zones of protoplanetary disks tend to be cleared. This process can be due to several factors, mainly by photoevaporation due to the stellar irradiation, or the formation of (proto)planets that tend to generate gaps around them. During this phase, disks are *transiting* from a more gaseous composition to a planetary system or a debris disk, and are classified as **transition disks**.
These disks were initially discovered looking at their SED shape, that shows lack of near-IR flux for $\lambda < 10\,\mu m$ (Wolk and Walter, 1996; Strom et al., 1989), but a clear definition of a transition disk doesn't still exist. Other authors define as transitional the disks that are optically thin in the near and mid-IR (Luhman et al., 2009). On the other hand, the far-IR excess is often still present. Since the dust that lies in the inner AU of the disk is hotter, it emits at higher frequencies (near-IR) than the dust farther from the central star, which is cooler and emits in the far-IR. The lack of near-IR radiation in the SED is so a proof of a gap in the dust distribution in the inner AU of the disk.
The incidence of transition disks on the total seems to be between 10% and 20%, but this depends first of all on the given definition. Moreover, the considered samples can suffer of selection effects, and also the spectral type of the star may cause misunderstandings in the SED interpretation. Anyway, their relatively low percentage can be interpreted in two ways: or the transition phase is uncommon or it occurs in very rapid times. The last one seems the most accepted, since there are no known physical processes able to dissipate the gas at all the radii simultaneously. So the transition phase must be very short, of about $0.5 - 1$ Myr, considering that the typical lifetime of a protoplanetary disk is between 5 and 10 Myr. This consideration gives important restrictions on the models for the processes of grain growth and planetesimals/planets formation.
Let's have a look at the main processes considered as responsible for the inner disk cleaning.

1.4.1 Grain growth and planet formation

During their motion, dust grains in disks can collide between themselves, giving arise to a growth process. As the grain dimension increases, their motion tends to be no more well-coupled to the gas one, leading to a separate evolution. Bigger grains tend to migrate towards the midplane of the disk, where the density is higher. Here they can collide between themselves and produce even bigger structures.
If this growth could progress undisturbed, the disk would be depleted of its smaller grains (size $< 100\,\mu m$) in very short times of about 10^4 yr. Since even in older disks these components are observed, there must be some type of material shuffling that slows the grain growth, or some kind of erosion or fragmentation processes in collisions (Dominik and Dullemond, 2008). Several theoretical problems seem to afflict the grain growth: for example, when they reach the size of about a meter, simulations seem to favor destructive processes in collisions instead of agglomeration (Brauer et al., 2008). A way to further proceed with their growth can occur via

vortexes or rings formation. These structures favor dust accumulation in restricted zones, increasing the collision probability, hence the formation of bigger bodies inside them.
Anyway, asteroids in solar system are a proof that bigger bodies can form, until reaching dimension well beyond a kilometer: these are called *planetesimals* and can also aggregate to form terrestrial planets or giant planet cores. The composition of planetesimals and protoplanets depends mainly on the location of the dust that forms them: near the star only heavy materials like iron or nichel can survive in dust aggregations, due to the higher temperatures. Looking at more external zones, the quantity of silicate grains and grains with ice increases, modifying also the composition of planetesimals they will form.
Finally, if a planet is far enough from the central star, it has higher possibilities to capture the surrounding gas and to form (and maintain) an atmosphere, becoming a giant planet (like the external planets in Solar system).
Several observations and simulations (Paardekooper and Mellema, 2004; Zhu et al., 2011; Dong et al., 2015b) show that a planet with a mass if $1\,M_J$ or higher is able to open a cavity in the gas distribution, while a lower mass planet ($0.1 - 0.2\,M_J$) is sufficient to remove the dust component around it. This is a typical situation that can verify in a pre-transitional or transitional disk, especially if a complete planetary system is forming inside it.

1.4.2 Photoevaporation

In some cases, the evolution of a protoplanetary disk can be mainly driven by high mass-loss rate due to photoevaporation. This would change the value of the surface density of the disk, especially in the zones where the gas is less gravitationally bounded. The photoevaporation is dependent on the intensity and on the spectrum of the stellar radiation; even stars external to the system can cause it, if they are sufficiently close or if they have strong UV emission (like O-B stars).
The stellar radiation heats up the gas in a tiny layer on the disk surface, such that $T_S > T_{eff}$, as calculated in Section 1.3.6. The gas sound speed c_s will equal the keplerian velocity at the radius

$$r_g = \frac{GM_*}{c_s^2} \tag{1.38}$$

For $r \sim r_g$ the gas results unbound from the disk and can separate from it. This causes a loss of surface density equal to

$$\dot{\Sigma}_{wind}(r) \simeq \mu c_s(r) n(r) \tag{1.39}$$

where μ is the mean molecular weight and $n(r)$ the numeric density of the gas at the base of the heated layer (Armitage, 2011). In reality, this process can occur even at $0.1 - 0.2\,r_g$, considering more accurate hydrodynamic models (Waters and Proga, 2012) and disk rotation (Liffman, 2003).
Let's consider only the photoevaporation due to the central star of the system. This is more efficient at smaller radii, since the flux scales as r^{-2}.
The responsible radiation is usually divided in three wavelength intervals:

- **Far UV (FUV)**, which photons have energy in the range $6\,eV < E < 13.6\,eV$. This radiation is able to dissociate molecular hydrogen (H_2).

- **Extreme UV (EUV)**, which photons have energy $13.6\,eV < E < 100\,eV$. This radiation is able to ionize atomic hydrogen.

- **X-ray radiation**, which photons are extremely energetic, $E > 100\,eV$.

The FUV and the X-ray radiation are more efficient in the earliest phases of disk life, and they can produce relevant mass loss for radii $r > r_g$. The EUV radiation effect peaks at $r \simeq r_g$, but the mass loss produced isn't very important in the initial phases (Gorti and Hollenbach, 2008).
Considering evolutionary models that include both viscosity and photoevaporation, it seems that EUV radiation assumes an important role after the star mass accretion decreases (Clarke et al., 2001). After its drop, an inner gap opens in the disk, when it is optically thin. This can extend from few up to about 10 AU, depending on the intensity of the radiation, and it is the main feature that characterize the *transition disks*.
Finally, when this gap is opened, the external disk is directly exposed at the EUV and X-ray radiation, that clean the disk in very short timescales of about $0.5 - 1$ Myr. This phase is called *disk dispersal*. After this, typically only a *debris disk* is left, where planetesimals and/or planets could have already been formed.

1.5 Large scale structures

In the last years several high resolution observations, mostly done with ALMA, revealed the presence of **large scale structures** in protoplanetary disks. For example, in HL Tau disk (Figure 1.3) a series of rings are easily recognizable in the millimeter continuum. These trace the distribution of millimeter-sized dust particles along the disk, revealing that the brighter regions are optically thick, and that the darker ones are optically thin. The first theory to explain this differentiation is to assume grain growth processes and/or planet formation in the darker regions, even if planets weren't directly detected. So these structures result to be very useful in understanding the formation of multiple planetary systems (as the Solar one), and represent a completely new field of research in the protoplanetary disks ambit.

Different types of *azimuthal asymmetries* have been revealed other than rings: in the Figure 1.4, it's possible to see a plethora of these structures, such as horseshoe-shaped concentrations, gaps, shadows, spiral arms (that can be single or multiple) or other irregularities in the *mm*-sized dust distribution. Depending on the disk, its other components, such as micron-sized dust or gas, can have different distributions since some processes internal to the disk can affect only one or some of them.

The origin of several of these structures is still unknown, or not confirmed. The formation of planets seems to be one of the main causes for the origin of gaps or also spiral arms. Indeed, their presence tends to create local pressure maxima and **vortexes** that act as *dust traps*, letting to the formation of rings and horseshoe-shaped accumulations. Also the planet migration can have important consequences on the

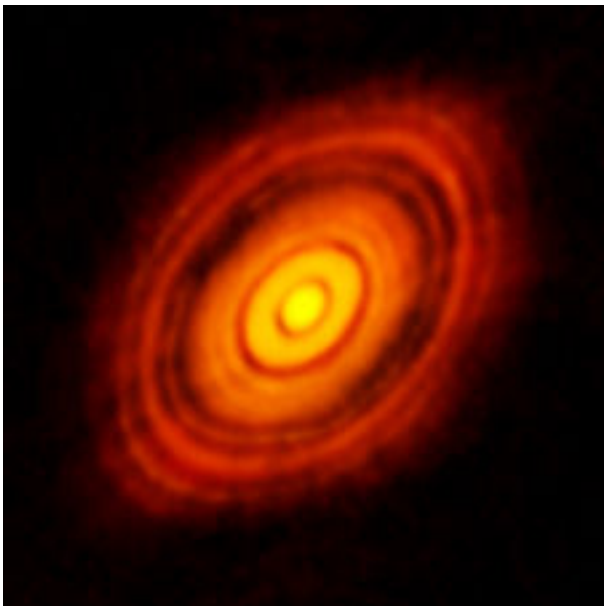

Figure 1.3: Continuum images in the *mm* range of the protoplanetary disk HL Tau, observed by ALMA. The multiple ring structure is clearly visible. Image by Brogan et al. (2015).

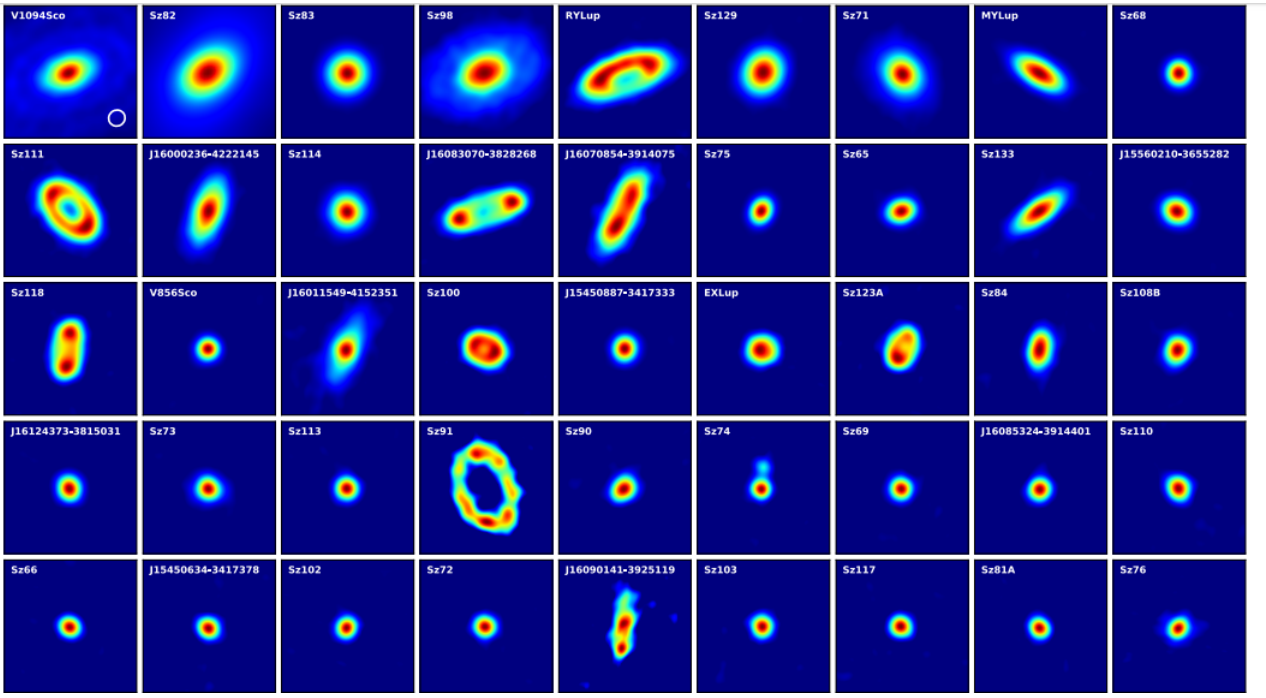

Figure 1.4: Images from ALMA (*mm* continuum) of some disks in the Lupus star-forming regions (image from (Ansdell et al., 2018)). In some of them it's possible to see large-scale structures in the dust distribution.

formation and maintenance of these structures.
Other mechanisms that were proposed to explain their formation are:

- **outbursts** from the main star(s): these can heat up the material at a certain distance, increasing the aspect ratio of the disk locally; this would put in shade the material behind it, that would be cooler and so closer to the midplane, until the disk height raises again enough to let the material to be illuminated again by the star. This *self-shadowing* effect can happen multiple times, generating alternate series of bright and dark rings, as in HL Tau.

- Presence of multiple **disks with different inclinations**, that can generate shadows on the external ones. This seems to be the case of the system that will be studied later, see Section 2.2.

- The presence of **unseen companion(s)**, or the interactions with external stellar systems, both for gravitational disturbances and photoevaporation effects, if their radiation is strong enough (for example for O-B external stars).

- **Self-gravity**: if (part of) the disk is enough massive or cold, a perturbation may grow under its non-negligible effect. This can lead to the formation of spiral arms, due to gravitational torques, or to the *fragmentation* of the disk.

Typically, it's difficult to establish whether these structures are precursor or consequences of planets formation. Their formation seems to be favored by the presence of planets, but it's also true that these accumulations of dust would favor the formation of planetesimals, and then of planets.
Moreover, the different asymmetries can cause or interact with each other, or can be due to a mixture of the previous phenomena, and usually it's difficult to determine what process is dominant in their formation and/or sustaining. Several hydrodynamical simulations, such as the ones performed in Chapter 4, are performed in these last years, and will be fundamental for understanding their nature.

1.6 Disk truncation

Let's consider a binary stellar system, with both the components in a pre-main sequence stage. This system can have three different disks, two circumstellars and one circumbinary. For simplicity, let's assume the disks to be geometrically thin and coplanar with the orbit plane of the binary. Also let's assume their evolution to be mainly driven by viscosity and gas pressure, and not by self-gravity (so to be relatively low massive).
For a binary system with a certain eccentricity and a non-extreme mass ratio, the disks will suffer a **truncation process**. The cause depends on the eccentricity of the system (Artymowicz and Lubow, 1994):

- for a circular orbit, **non-resonant** (or **tidal**) interactions arise from the creation of tidal distortion in the disk parts nearest to the secondary star. The torque that is generated in this way is dependent on the viscosity of the disk.

- When the orbit is elliptical, **resonant** interactions result in excitation of density waves at Lindblad resonances. These are orbital resonances in which the *epicyclic frequency*[4] of an object is a multiple of some *forcing frequency*.

In both cases, there is a transfer of angular momentum in the outward direction.

The result of such interactions is the opening of a gap in a circumbinary disk, and of a truncation in a circumprimary or circumsecondary disk. For the first case, the radius where the gap opens is the one at which the total external torque T equals the viscous stresses. Lin and Papaloizou (1986) calculated it as

$$3\pi\,\alpha\left(\frac{H}{r}\right)^2 = \frac{T}{\Sigma\,\Omega^2\,r^4} \tag{1.40}$$

where α is the coefficient used in the Shakura-Sunyaev prescription for the viscosity ν (Eq. 1.15) and the value of Σ is calculated at the corresponding radius. In this equation, the left term represents the inverse of the Reynolds number Re^{-1} of the gas (times 3π) and measures the viscous stresses (see Section 3.1.4). On the right side there is instead the specific resonant torque. When the first term is lower than the second, the resonant torques prevail and the gap is opened under a certain radius.
A one more condition is needed, and it regards the opening time of the gap, which is of the order of $t_{open} = (\Delta r)^2/\nu$, where Δr is the radial extent of the gap. This must be shorter than other timescales such as the disks lifetime and the orbital evolution of bodies, in order to reach the balance between viscous and resonant torques.

Let's look now at the truncation of circumstellar disks, around both the stars. Let's consider for example two stars in a circular orbit, with a reduced mass[5] of $\mu = 0.3$. The resulting radius at which the circumprimary disk is truncated is at about $0.4\,d$, with d the distance between the two stars in the binary system. This result comes both from free-particle orbital calculations, done by Paczynski and Rudak (1980); and from the work of Papaloizou and Pringle (1977) which follows the previous approach of equating viscous and tidal torques. Regarding the circumsecondary disk, its extension results to be between $0.20\,d$ and $0.27\,d$, considering the respective works. This larger uncertainty is due to relevant non-axisymmetry in these disks, that results more evident than in circumprimary ones. In any case, this value is about 90 % of the value of the average Roche lobe radius for each component (Papaloizou and Pringle, 1977). This gives an upper limit for the extension of the circumstellar disks in a binary system with a circular orbit.
When the parameter μ increases, so when the secondary star has higher mass, the effect on the circumprimary disk is the reduction of its truncation radius. This happens because the higher the mass of the companion, the stronger will be the resonant torques acting on this disk, so the equilibrium with the viscous stresses will be reached in more internal zones. On the contrary, the truncation radius for

[4] It is the frequency of radial motions due to a small perturbation in the orbit of a body.

[5] With this notation it's supposed the total mass of the system to be $M_{TOT} = 1$, the mass of the primary star $M_1 = 1 - \mu$ and the mass of the secondary $M_2 = \mu$.

Reduced mass	$\mu = 0.3$				$\mu = 0.1$			
Eccentricity/ Viscosity	$e = 0$	$e = 0.2$	$e = 0.4$	α	$e = 0$	$e = 0.2$	$e = 0.4$	α
Primary disk	0.40	0.24	0.17	10^{-4}	0.47	0.28	0.21	10^{-4}
		0.28	0.21	10^{-2}		0.35	0.26	10^{-2}
Secondary disk	0.24	0.17	0.12	10^{-4}	0.18	0.12	0.09	10^{-4}
		0.20	0.15	10^{-2}		0.14	0.10	10^{-2}

Table 1.1: Values of the truncation radius (in units of the semimajor axis a) of the circumstellar disks for some configurations of the binary system. The values are taken from Figures 5-8 in Artymowicz and Lubow (1994) paper.

the circumsecondary disk will increase: the effect of the primary star on it is symmetric to the one already described, and an increase of μ would mean a decrease of $M_1 = 1 - \mu$. As a consequence, the resonant torques are less effective on the disk, and the balance with the viscous ones is reached at higher radius.
When the orbit is eccentric, instead, some other resonances with high power of e in their calculations play a more important role in determining the size of the circumstellar disks. As the eccentricity of the system increases, the radius of both the disks tends to decrease, meaning that the resonant torques are stronger. Artymowicz and Lubow (1994) found that for an eccentric orbit of the binary system the truncation radius is depending also on the viscosity of the disk, considering an α-prescription for it. Fixed the eccentricity, the higher the value of α, the larger will be the disk (around both stars). This is intuitively reasonable since when α increases, so when the disk is characterized by an higher viscosity, the torques generated by the resonances will be balanced at higher radii.
In the Table 1.1 some values of the truncation radius in units of a are shown, with a representing the semimajor axis of the binary orbit. It is possible to see its dependences on the parameters just explained.

Chapter 2

The HD100453 system

2.1 The Herbig star and the dwarf companion

The system studied for this thesis work, and on which the hydrodynamical simulations are applied, is named HD100453. This is located at the coordinates $\alpha = 11°33'5''$ and $\delta = -54°19'28''$ (J2000), in the Lower Centaurus Association (data from *Simbad*), at a distance of 114^{+11}_{-4} pc (Benisty et al., 2016).
The primary object, HD100453 A, is an Herbig star; its spectral class is A9Ve. It's a very young star, with a mass of $M \simeq 1.7\, M_\odot$ and a luminosity of $L \simeq 9\, L_\odot$ (Wagner et al., 2015).
The presence of a companion was confirmed by the observations provided by Collins et al. (2009): this star, named HD100453 B, is a dwarf star (M4V-M4.5V class), distant ~ 119 AU from the main star, with a mass of $0.2 - 0.3\, M_\odot$.

2.1.1 Age of the system

Placing the main star on the evolutionary tracks for pre-main sequence (PMS) stars of that mass, Collins et al. (2009) found that its age is between 9 and 18 Myr. The study of the companion (assuming that both stars has formed from the same molecular cloud) restricts this interval, since its age, always based on its own evolutionary track, is estimated as 10 ± 2 Myr.
Another confirmation of the relatively old age of the system comes from the measurement of the mass accretion rate of the main star. This is derived looking at the excess of FUV continuum, normally present in active Herbig Ae stars, but in this system this continuum is almost missing, and the accretion rate is estimated as $< 1.4 \cdot 10^{-9}\, M_\odot/yr$ (Collins et al., 2009), at least 10 times lower than usual values for active Herbig stars. Moreover, the upper age limit set for the Lower Centaurus Crux Association is about 20 Myr (Mamajek et al., 2002); so the age of the system is established to be 10 ± 2 Myr.

2.2 Disk structures

Most of Herbig stars host protoplanetary disks, typically inferred through an excess of IR radiation in the stellar SED. Since these structures have typical lifetimes of $\sim$ 10 Myr, the disk in this system is relatively old, and is classified as a *transition disk*.
The observed protoplanetary disk is a circumprimary disk, so it's present only around the main star. There are two properties of immediate relevance:

1. being an old disk, its mass seems to be very low compared to the usual mass of a protoplanetary disk (about 10^{-4} $M_{\odot}$, from Benisty et al. (2016)), with a very low *gas-to-dust ratio* of about 4:1 (Collins et al., 2009), detected from the lack of CO lines in the outer disk. This is probably due to the formation of big dust grains and/or planetesimals inside the disk;

2. its tiny dimension: from the scattered light images we can't see almost no disk or structure beyond $\sim$ 45-50 AU, meaning that the disk has probably been tidally truncated by the companion, at about 1/3 of the distance of it from the main star (Section 1.6). This dimension is also confirmed by the presence of an other star at about 90 AU from the main object that doesn't belong to the system (its exclusion is based on the study of its proper motion), meaning that at this distance the disk must be already non-existing or really optically thin (Benisty et al., 2016).

This disk is of particular interest thanks to the presence of different structures inside it, as it can be seen in the Figure 2.1. Let's look at them in detail.

2.2.1 Spiral arms

One of the main features visible in the disk is the presence of a **two-armed spiral structure** departing from the main disk in an almost symmetric configuration: the angle between their departure points is $\sim 180°$. Looking at the Figure 2.1 it's possible to see their location: the widest and less luminous one is located in the North-East (NE) side, the less wide and most luminous one (twice the previous one) in the South-West (SW). The physical parameters characterizing them are reported in Table 2.1, and are taken from Benisty et al. (2016), and from Wagner et al. (2015). Since the arms opening direction is clockwise, and the position angle of the companion is $\sim 130°$ (Dong et al., 2015a), the SW arm is the one pointing to it.
The origin of these spiral arms seems to be due, at least partly, to the **gravitational instabilities induced by the companion dwarf**, as the simulations later discussed in Chapter 4 seems to reveal. Their differences in luminosity, wideness and opening angle are due to two principal factors:

- the symmetry is broken because the companion dwarf is present only at one side of the disk, so it induces different gravitational forces on the two arms. The simulations seems to detect this asymmetry. Moreover the illumination of the companion on the two spiral arms is different;

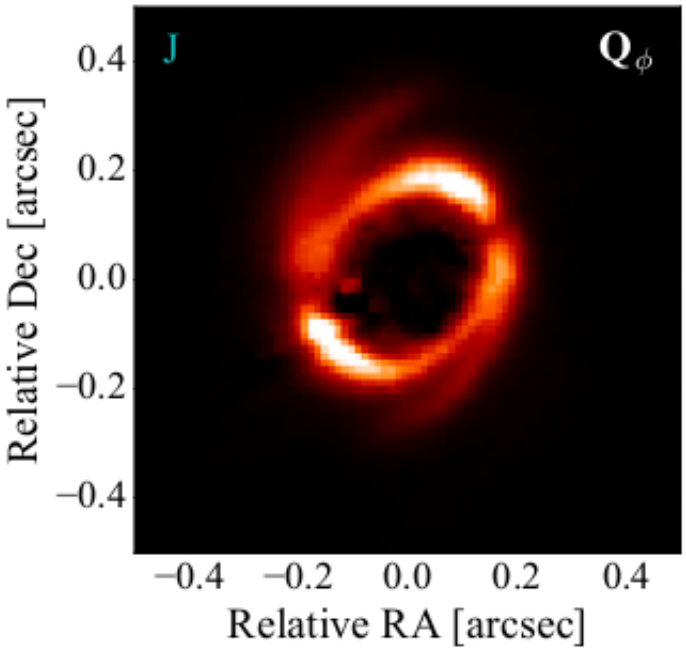

Figure 2.1: J-band scattered-light image of the HD100453 disk, from Benisty et al. (2016). It is possible to see at all the structures present in this disk, described in Section 2.2. In this image, North is pointing up and East left.

- the disk is inclined of $\sim 30°$ from face-on (Benisty et al., 2016; Wagner et al., 2015, 2018). This implies that one side of the disk is nearer to us than the other, and this contributes to the production of these differences.

Regarding the second point, the SW arm seems to be the nearest to us, since its opening angle is more narrow. Moreover, the higher luminosity is due (at least partially) to the projected superposition of the dust particles scattering the light on the surface of the disk. These effects are reflected, on the contrary, on the NE side: the arm is more widespread since it's possible to see a bigger part of it (so the luminosity is lower), and the opening angle is larger.
Another feature that seems to confirm the vicinity of the SW side is the presence of another structure, qualitatively similar to a spiral arm, on the same side (Benisty et al., 2016). This is a much fainter source, which presence can be predicted through radiative transfer models, if it's supposed to trace the light scattered by the dust particles on the surface of the *bottom* side of the disk. This feature wouldn't be

Table 2.1: Parameters characterizing the two spiral arms in HD100453 disk

Spiral arm	NE	SW
Disk intersection	22°-79°	194°-251°
Extension (angle)	−15°	155°
Extension (AU)	48 AU	39 AU
Opening angle	38°	30°
Luminosity	L	2L

possible to see if the disk was on a *face-on* configuration, and the NE counterpart can't be seen since it's hidden by the main disk.

2.2.2 The ring and the shadows

Looking more at the inner zones of the disk surrounding HD100453A, it's noticeable the presence of the main structure of the disk: a **ring** that extends from $\sim$ 16 AU to 21-29 AU, depending on the angle at which it's observed. The most accepted value for its inclination is 28° (Wagner et al., 2018).
The ring brightness is variable along the azimuthal coordinate, with two maxima at $\sim$ 135° and at $\sim$ 325° that have a wideness of $\sim$ 70°[1]. On the contrary, there are two minima at $\sim$ 100° and at $\sim$ 293° (Benisty et al., 2016): these are called **shadows** and are very narrow regions across the ring, from which the spiral arms seems to depart. It's not actually clear whether this last point is just a coincidence or if the shadows have some type of influence on the spiral arms formation and/or location.
In these regions the pressure and the temperature of the gas are lower, since they are less irradiated by the star. This bring the gas to flow down to the *midplane* of the disk, and the *scale height* is reduced in these zones.
This change of pressure leads to an azimuthal acceleration of the gas when it crosses the shadows; combining this effect with the differential rotation of the disk, it's possible to trigger the spiral arms, but this also requires the cooling timescale to be much shorter than the dynamical timescale, in order to let the gas to feel the pressure gradient (Montesinos et al., 2016).
Today it's not clear whether the shadows are steady or moving: a way to constrain this, assuming that the spirals are generated by the shadows, is to reveal the rotation direction of these ones (Benisty et al., 2016).
A possibility for the formation of the shadows could be the presence of an inner disk in the closest zone of the system, as will be discussed in the next section.

2.2.3 The cavity and the inner disk

Under $\sim$ 16 AU, the intensity of the scattered light images suddenly drops, revealing a **cavity**. This seems not to be present until the star, since there is a relevant near-IR excess in the SED of the system in the very internal AU, revealing the presence of an **inner disk** very close to the main star. The inner working angle of several articles (Benisty et al., 2016; Wagner et al., 2015, 2018) gives an upper limit of the extension of this inner disk of 10 AU.
About the formation of the internal cavity, the presence of an unseen companion is the most likely scenario. This must be a planet, or a brown dwarf, that tends to clean its surrounding zone accumulating mass on itself or pushing the material far away from itself. Some simulations concerns this aspect of the disk and will try to reproduce putting in this zone of the disk a planet with different mass and/or distance from the main star (Section 4.2).

[1] Angles are counted in the counterclockwise direction starting from the North.

The main feature of the inner disk, instead, is its *misalignment* with the rest of the system, of about $\sim 70°$ (Benisty et al., 2016; Wagner et al., 2018). This is inferred from the wideness of the shadows in the ring, which creation seems to be due to the presence of this inclined inner disk, that obscures the illumination of the main star on some zones of the major disk (so of the ring).
What remains unclear is the origin of the misalignment of this zone: several theories were made, but no one has been completely confirmed. The inclination of this disk could be due to gravitational instabilities induced by the unseen companion inside the hole, or by the eccentric orbit of the companion star.
Another way that was proposed to explain its origin is to suppose that the companion star wasn't originated by the initial molecular cloud from which HD100453 A and the disk formed: if the companion was captured after the formation of the system, its different inclined orbit could have bring the external disk on its same orbital plane, while the internal disk could remain on its initial configuration. However, looking at the rotation axis of the star, supposing its rotation should be around 150-200 km/s and its inclination about 30°, this hypothesis seems to be discarded, and the most probably configuration is the one with the inner disk as the only misaligned body in the system (Wagner et al., 2018).
Anyway, the simulations later discussed in Chapter 4, being just 2-dimensional, are not able to reproduce this kind of feature, and neither the shadows will be seen. They can instead try to find an upper limit to the external radius of the inner disk, looking at the inner radius of the gap generated by the planet in the cavity.

2.3 Other similar sources

In the last years, high resolution images of protoplanetary disks revealed the presence of different structures in them, on different scales, such as multiple rings (in HL Tau, for example, ALMA (2015); or cavities, typically generated by planets that tend to clean their surrounding zones; or shadows, as in HD142527 (Avenhaus et al., 2014). Other sources that shows spiral arm features are SAO206462 and MWC758 (shown in Figure 2.2), both with an almost symmetric configuration of the arms as in HD100453 case (Dong et al., 2015a). But while for the last one the presence of the companion star seems to be the main cause for the spirals generation, for these other two systems a similar source has not been found.
So the question that raised in these years is: how can this type of structure be triggered and maintained in time? Several theories have been proposed:

- at first, unseen planets or brown dwarfs were supposed to be responsible for their formation. But a companion with this relatively low mass is able to generate just one arm, and producing a double spiral pattern would require the presence of two planets with very specific ratios in mass and orbital period, in a very unlikely and unstable configuration (Dong et al., 2015a). Moreover, even the pitch angles of the arms would be different;

- they can be induced by self-gravity of the disk, but only if the disk mass is high enough ($M_{disk} \geq 0.1 M_\star$) the instabilities can be able to trigger the spirals. This seems not to be the case for the three systems cited (Dong et al., 2015a);

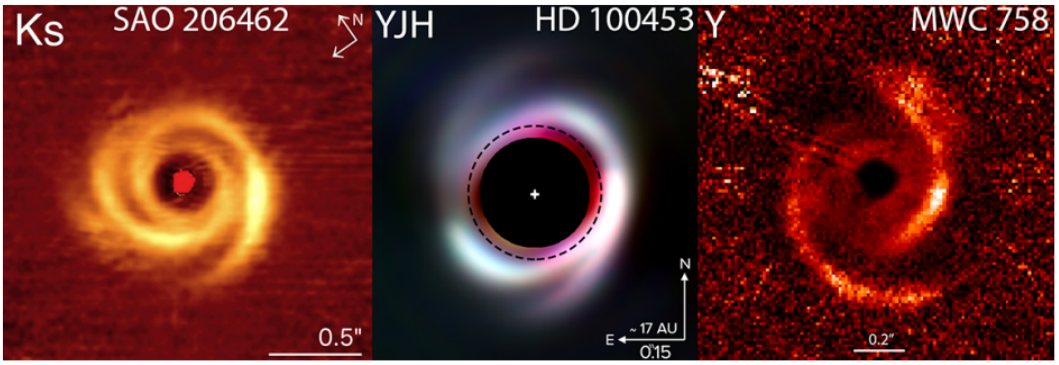

Figure 2.2: Spiral arms in the SAO206462, HD100453 and MWC758 disks, all showing their double symmetric pattern. The images are taken in different bands, or superposition of them, and the contrast is adapted to get similar intensities (Wagner et al., 2015).

- presence of shadows in the main disk. These shadows, as already explained, can generate instabilities and density waves because of the pressure drop that characterize them. But not always these shadows have been detected, and moreover the formation and maintaining of the spirals can depend on the stability/rotation of the shadows. The studies for this type of mechanism for triggering spirals are still at the beginning, but it seems to be able to explain the double symmetric spiral pattern (Montesinos and Cuello, 2018).

Chapter 3

FARGO3D code and simulations setups

In this chapter are given a brief description of the code used for the hydrodynamical simulations performed (Section 3.2), and later are explained the setups and the initial conditions that have been adopted (Section 3.3).
Before doing that, let's resume some general notes about the theory of gas motion.

3.1 Hydrodynamical equations

3.1.1 Ideal gas

The material that composes a protoplanetary disk can be treated as a fluid, since it's mainly gaseous (about 99% gas and 1% dust) and since the mean free path of the particles λ is much lower than the radius R of the disk. Moreover, its density and pressure are very low, so the gas can be considered as perfect.
This gives the possibility to formulate its *equation of state*, the relation connecting its pressure P and its density ρ, as:

$$P = \frac{\rho k_B T}{\mu} \tag{3.1}$$

where T is the gas temperature, $k_B = 1.36 \cdot 10^{-16}\, erg/K$ is the Stefan-Boltzmann constant, and μ is the mean molecular weight of the gas ($\mu = 1.67 \cdot 10^{-24}\, g$ for a gas composed only by atomic hydrogen).
Another important relation is the one between the pressure and thev internal specific energy e of the gas:

$$P = (\gamma - 1)\rho e \tag{3.2}$$

where γ is the adiabatic index of the gas. This depends on the degrees of freedom of the gas, and equals 5/3 for monoatomic gas and 7/5 for diatomic gas.
For an adiabatic compression or decompression of an ideal gas, the pressure and the density are related as

$$P = K\rho^{\gamma} \tag{3.3}$$

where K is a constant in an adiabatic process, and it is related to the entropy of the considered gas.
Moreover, the *adiabatic* and the *isothermal speed of sound* are defined respectively as:

$$C_s^2 \equiv \frac{\partial P}{\partial \rho} = \gamma \frac{P}{\rho} = \gamma(\gamma - 1)e \tag{3.4}$$

$$c_s^2 \equiv \frac{P}{\rho} = (\gamma - 1)e \tag{3.5}$$

It is to notice that in isothermal processes the parameter K is no more a constant, while e it is, since the gas is immediately brought to a specific ambient temperature by some source (for example star radiation).

3.1.2 Equation of motion

The motion of the gas contained in a certain volume V is governed by some fundamental equations: the continuity equation, the Euler equation, and the energy conservation equation.
The Eulerian approach consists in studying the evolution of the properties of the whole gas contained in a control volume V, which surface can be denoted as $\partial V \equiv S$. Let's define $\vec{n}$ as the vector that points out from every infinitesimal surface element dS (Figure 3.1). So it is possible to express the conservation equations as follows[1].

- The **continuity equation**, also referred as **mass conservation equation**:

$$\frac{\partial}{\partial t}\int_V \rho \, dV = -\int_{\partial V} \rho \, \vec{u} \cdot \vec{n} \, dS \;\Rightarrow\; \frac{\partial \rho}{\partial t} = -\nabla \cdot (\rho \vec{u}) \tag{3.6}$$

  It states that the variation of mass in a volume V must be balanced by an inflow or outflow of material (with velocity $\vec{u}$) through the surface ∂V.

[1] The equations are expressed on the left in their integral form and on the right in their differential one. The passage from one to another is possible through the Gauss theorem.

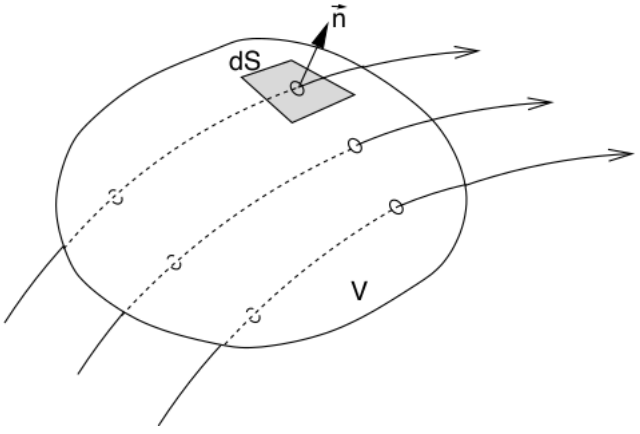

Figure 3.1: Example of control volume, with all the quantities considered in the equations in Section 3.1.2.

- The **Euler equation**, also referred as **momentum conservation equation**:

$$\frac{\partial}{\partial t}\int_V \rho\vec{u}\,dV = -\int_{\partial V}\rho\vec{u}\,\vec{u}\cdot\vec{n}\,dS - \int_{\partial V} P\vec{n}\,dS \Rightarrow$$

$$\Rightarrow \frac{\partial(\rho\vec{u})}{\partial t} = -\nabla\cdot(\rho\vec{u}\,\vec{u}) - \nabla P \quad (3.7)$$

  It states that the variation of momentum ($\rho\vec{u}$) is equal to the inflow or outflow of momentum through ∂V (first term on the right side); at this must be added the contribution of forces external to the control volume (like the gravitational one), which generate the pressure P present in the second term on the right.

- The **energy conservation equation**:

$$\frac{\partial}{\partial t}\int_V \rho\left(U+\frac{u^2}{2}\right)dV = -\int_{\partial V}\rho\left(U+\frac{u^2}{2}\right)\vec{u}\cdot\vec{n}\,dS - \int_{\partial V} P\vec{u}\cdot\vec{n}\,dS \Rightarrow$$

$$\Rightarrow \frac{\partial}{\partial t}(\rho e) = -\nabla\cdot[(\rho e + P)\vec{u}] \quad (3.8)$$

  where U is the specific internal energy and $u^2/2$ the specific kinetic energy of the gas; e is their sum, that gives the gas energy when multiplied by ρ. This equation states that the variation of energy is equal to the advection of energy through the surface ∂V (first term on the right side) added to the work done by forces external to the control volume (second term on the right side).

3.1.3 Special cases

When the considered gas is characterized by some special properties, the equations above described can be simplified.
For example, if the gas flow is relatively smooth (which means there are no shocks) and if there aren't heating or cooling processes, the system is *isentropic*. In this case, the energy equation isn't necessary to calculate. The pressure and the density are simply related by Eq. 3.3, where K remains constant.
On the opposite, let's assume an extremely heating/cooling rate process, that occurs in much less time than the dynamical timescale. In this case the gas is maintained at a certain temperature T, so it is *isothermal*. The energy e assumes a constant value, and from Eq. 3.2 it can be seen that there is a simple proportional relation between the gas pressure and density.
Finally let's consider the case of a highly supersonic flow, which means that the pressure is negligible compared to ρu^2. In this case the continuity equation doesn't change, while the energy conservation equation becomes irrelevant because $e \simeq 0$. The momentum equation reduces to

$$\frac{\partial(\rho\vec{u})}{\partial t} = -\nabla\cdot(\rho\vec{u}\,\vec{u}) \quad (3.9)$$

and describes the gas flow together with the continuity equation (3.6) in a simplified way.

3.1.4 Fluid viscosity

Let's consider a fluid that has a not negligible viscosity. This property leads to a modification in the pressure term of the momentum equation (3.7). Through tensorial calculation, it can be seen that non-diagonal components of the pressure tensor (that substitutes ∇P) can be different from 0. This leads the transport of arbitrary momentum component in every direction, while this isn't true in non-viscous fluids (momentum along x-direction is always transported along the x direction, for example). The modified equation takes the name of *Navier-Stokes equation*.
Moreover, in a viscous fluid every compression or decompression causes a loss of energy of the system (processes aren't reversible).
A way to identify how much the viscosity can be relevant in describing the motion of a fluid is through the **Reynolds number**: this is simply the ratio between the inertial and the viscous forces that act on the fluid, and is expressed as

$$Re = \frac{uL}{\nu} \tag{3.10}$$

where u is the velocity of the flow, L is a typical size of the fluid in the analyzed system, and ν is the cinematic viscosity of the fluid. This number can be very variable depending on the considered scales and on the properties of the fluid and of the flow. When $Re \gg 1$, so when inertial forces prevail, the flow is in a *turbulent regime*; on the contrary, if $Re \ll 1$ the fluid is viscous and in a *laminar regime*.
In a turbulent regime, hydrodynamical calculations are more complicated, because the turbulence can establish at different scales (the so-called *turbulent cascade*) until it vanishes at values of L for which $Re \simeq 1$. Moreover, even turbulence can be a source of viscosity in the fluid.

3.2 The FARGO3D code

Several codes have been developed in order to analyze and calculate the motion and the properties of gas and/or fluids in a system through the **hydrodynamical equations (HD)**, or **magnetohydrodynamical equations (MHD)** if also the magnetic fields play a significant role in the physical problem to analyze.
The one used for this thesis work is named FARGO3D, which was developed especially for structures like protoplanetary disks by Pablo Benitez Llambay and Frèdèric Masset[2].
The code, given a certain set of parameters, initial conditions and boundary conditions, solves the *continuity*, the *Navier-Stokes* and the *energy equation* (see Section 3.1.2) for every cell of a grid, that can be in a 1D, 2D or 3D frame. The outputs are binary files generated at every time step DT, given as a parameter in the code. These files can then be converted in opportune matrices that represents distributions of specific physical quantities, such as density, pressure or velocity fields.

[2] All the informations about the structure and the properties of the code are referred to the article by Benítez-Llambay and Masset (2016) and to the FARGO3D manual

3.2.1 Equation solving methods of FARGO3D

The code is able to solve the HD equations in three different coordinates sets (defining the location of a single cell):

- cartesian: the X, Y and Z coordinates correspond to the x-axis, y-axis and z-axis;
- cylindrical: the X, Y and Z coordinates correspond to the azimuth angle φ, the radius R and the height z;
- spherical: the X, Y and Z coordinates correspond to the azimuth angle φ, the radius R and the colatitude θ[3].

Depending on their nature, the physical quantities can be defined in the center of a cell (**centered**) or on its edges (**staggered**): for example, the internal energy and the density, which are scalar, are centered; while the velocity, which is vectorial, is staggered.

The equations that are solved by the code are the following (in Eulerian coordinates):

- the **continuity equation** (Eq. 3.6);
- the **Navier-Stokes equation**, which is a modified version of the *momentum conservation equation* (Eq. 3.7):

$$\rho\left(\frac{\partial\vec{u}}{\partial t} + \vec{u}\cdot\nabla\vec{u}\right) = -\nabla P + \nabla\vec{T} + \vec{F}_{ext} - \rho\left[2\vec{\Omega}\times\vec{u} + \vec{\Omega}\times(\vec{\Omega}\times\vec{r}) + \dot{\vec{\Omega}}\times\vec{r}\right] \tag{3.11}$$

  where $\vec{F}_{ext}$ is an external force, such as the gravity force; the terms containing $\vec{\Omega}$ are the fictitious forces arising from having a non-inertial system that rotates with constant angular velocity $\vec{\Omega}$; and $\vec{T}$ is the *viscous stress tensor*, which depends on the kinematic viscosity ν of the disk, and is expressed as

$$\vec{T} = \rho\nu\left[\nabla\vec{u} + (\nabla\vec{u})^T - \frac{2}{3}(\nabla\vec{u})\,\vec{I}\right] \tag{3.12}$$

  where ν is the viscosity of the gas, and $\vec{I}$ the unit tensor.
  Other terms are involved, but they include magnetic fields, which weren't considered in this thesis work;

- the **energy conservation equation** (Eq. 3.8). In the FARGO3D code it is a non-conservative formula.

An *equation of state* is also added, in the *isothermal* (3.13) or in the *adiabatic* (3.14) form:

$$P = c_s^2\rho \tag{3.13}$$

[3] In the cylindrical and in the spherical sets, the X coordinate is periodic.

$$P = (\gamma - 1)\rho e \tag{3.14}$$

where c_s is the isothermal speed sound, and γ the adiabatic gas index.
FARGO3D can solve these differential equations with the *finite differences* method, where the derivatives are approximated as finite differences in tiny intervals; or with the *finite volume* method. The equations, which have the general expression

$$\frac{\partial \vec{Q}(\vec{x},t)}{\partial t} + \nabla \vec{Q}(\vec{x},t) = S(\vec{x},t) \tag{3.15}$$

are typically split in two sub-equations, and then the total solution is a linear combination of the two. The first equation contains the time derivative and the **transport term**, which is the one with the gradient of the physical quantity $\nabla \vec{Q}(\vec{x},t)$; the second one contains the time derivative and the **source term**, expressed by $S(\vec{x},t)$.
Starting from a time t_0, the code calculates the solution for the source equation, it improves it in the transport one and finds the solution at time $t_0 + \Delta t$, that will be used as the initial condition for the next step.

Source equation

The source term $S(\vec{x},t)$ is a component of the Euler and the energy equations that can include pressure gradients, gravitational and viscous forces, and the work done by pressure forces. To be solved, the source equation is divided into sub-steps. In the first of them the velocity fields are updated by gravitational forces and pressure gradients. In a cylindrical reference frame, as the one used for the subsequent simulations, the solved equations are:

$$\frac{\partial u_\varphi}{\partial t} = -\frac{1}{r\rho}\frac{\partial P}{\partial \varphi} - \frac{1}{r}\frac{\partial \Phi}{\partial \varphi} \tag{3.16}$$

$$\frac{\partial u_r}{\partial t} = -\frac{1}{\rho}\frac{\partial P}{\partial r} - \frac{\partial \Phi}{\partial r} + \frac{(v_\varphi^t)^2}{r} \tag{3.17}$$

$$\frac{\partial u_z}{\partial t} = -\frac{1}{\rho}\frac{\partial P}{\partial z} - \frac{\partial \Phi}{\partial z} \tag{3.18}$$

where (u_φ, u_r, u_z) are the velocity components in cylindrical coordinates, Φ is the gravitational potential and $v_\varphi^t = v_\varphi + \Omega\, r$ is the azimuthal velocity in an inertial frame. Note that the calculations of the potential and the pressure gradients is relatively easy thanks to the *staggering* of the velocity fields.
The next sub-steps add an artificial von Neumann-Richtmyer viscosity (taken from Stone and Norman (1992)) and the work of the pressure forces, if the energy equation is solved. A final sub-step is added to implement the viscous stress tensor in the velocity field calculation.

Transport equation

Let's consider a cell in the mesh of the code. This is uniquely identified with a set of indexes (i, j, k) along the used coordinate set, while its borders are labeled with the notation ($i \pm 1/2$, $j \pm 1/2$, $k \pm 1/2$).

Starting from the time step n, the transport equation calculates the variation of a physical quantity Q (so its value at the time step $n+1$) inside a control volume V as exclusively due to the flux of it through the surface ∂V, such as

$$\frac{\partial}{\partial t}\int_V Q(\vec{x},t)\,dV = \int_{\partial V} Q(\vec{x},t)\vec{u}\cdot\vec{n}\,dS \tag{3.19}$$

The numerical code applies a discretized version of this equation, that for a *centered* physical quantity Q_{ijk} can be expressed as:

$$\frac{Q^{n+1}_{ijk}-Q^{n}_{ijk}}{\Delta t}V = -\left[F_{X_{i+\frac{1}{2}jk}} - F_{X_{i-\frac{1}{2}jk}} + F_{Y_{ij+\frac{1}{2}k}} - F_{Y_{ij-\frac{1}{2}k}} + F_{Z_{ijk+\frac{1}{2}}} - F_{Z_{ijk-\frac{1}{2}}}\right]^{n+\frac{1}{2}} \tag{3.20}$$

where F is the flux of the physical quantity along a certain direction between the considered cell edges. The superscripts n and $n+1$ are indicative of the time steps at which Q is calculated.

3.2.2 The CFL condition

To guarantee the stability of the code, the integrated time over every set of sub-steps must be lower than a certain interval. It is the so called *Courant-Fridrichs-Lewy condition*: from a physical point of view, it establishes that information can't travel over more than one cell per time step. The formula for its calculation is

$$\Delta t = C\cdot\min\left[\left(\sum\nolimits_i \Delta t_i^{-2}\right)^{-1/2}\right] \tag{3.21}$$

where C is a constant value called *Courant number*, equal to 0.44 in the FARGO3D code. The single intervals equal to $\Delta t_i = \min_j(\Delta t_{i,j})$ where j is the radial or the azimuthal direction. The various $\Delta t_{i,j}$ correspond to

1. Sound waves: $\Delta t_{1,j} = \Delta_j / c_s$
2. Fluid motion: $\Delta t_{2,j} = \Delta_j / |u_j|$
3. Artificial viscosity: $\Delta t_{3,j} = 4\sqrt{2}\,|\Delta_j/\Delta u_j|$, where $\Delta u_j = u_{j_{l+1/2}} - u_{j_{l-1/2}}$ is the difference in the velocity between two adjacent cells along the j direction ($l \pm 1/2$ are the cell borders).
4. Viscosity: $\Delta_{4,j} = \Delta_j^2/(4\nu)$ with ν the kinematic viscosity.

3.3 Simulation setups

3.3.1 The `.par` file

FARGO3D provides different setups, depending on the configuration of the disk or the system that needs to be studied. Once that the `SETUP` has been chosen, it is possible to modify the main parameters of the system in the `SETUP.par` file of the code. An example of this, reported in Figure 3.2, shows its structure.

```
### Run only this parameter file is FARGO3D was build using the setup 'fargo'
Setup                   fargo

### Disk parameters

AspectRatio             0.05            Thickness over Radius in the disc
Sigma0                  6.3661977237e-4 Surface Density at r=1
Nu                      0.0             Uniform kinematic viscosity
SigmaSlope              1.0             Slope of the surface density
FlaringIndex            0.0

### Planet parameters

PlanetConfig            planets/jupiter.cfg
ThicknessSmoothing      0.6
RocheSmoothing          0.0
Eccentricity            0.0
ExcludeHill             no
IndirectTerm            Yes


### Mesh parameters

Nx                      384             Azimuthal number of zones
Ny                      128             Radial number of zones
Xmin                    -3.14159265358979323844
Xmax                    3.14159265358979323844
Ymin                    0.4             Inner boundary radius
Ymax                    2.5             Outer boundary radius
OmegaFrame              1.0005
Frame                   G

### Output control parameters

Ntot                    1000            Total number of time steps
Ninterm                 20              Time steps between outputs
DT                      0.314159265359  Time step length. 2PI = 1 orbit
OutputDir               @outputs/fargo

#Plotting parameters

Log                     yes
```

Figure 3.2: Original `fargo.par` file in the code. It shows several parameters regarding the disk, the planetary configuration, and the mesh and output options.

```
############################################################
#   Planetary system initial configuration
############################################################

# Planet Name   Distance (AU)     Mass    Accretion     Feels Disk     Feels Others
Planet          20.0              0.01       0.0           NO             YES
HD100453B       120.0             0.3        0.0           NO             NO
```

Figure 3.3: Example of a `.cfg` file, containing the list of planets and/or companions, with some of their characteristics and properties.

All the simulations done for this thesis work are **2-dimensional** and consider only the HD equations, without the presence of magnetic fields. The `fargo` setup adapts well for the HD100453 specific system.
The performed configuration consists in positioning the main star HD100453 A in the center of the mesh, surrounded by its protoplanetary disk (of which parameters are discussed in the next paragraph), and then add the dwarf companion HD100453 B as it was a planet in another file, described at the end of this section. Later also another massive companion has been put close to the main star, with the aim to reproduce the observed cavity described in Section 2.2.3.

Disk parameters

The first set of parameters regards the physical characterization of the gas in the protoplanetary disk at its initial conditions.
Considering a 2D model, the fundamental physical quantity to calculate is the **surface density**. Its equation is written in another file of the `SETUP`:

$$\Sigma(r, t_0) = \Sigma_0 \left(\frac{r}{R_0}\right)^{-p} \exp\left(-\frac{r}{R_C}\right) \tag{3.22}$$

which is a typical power-law profile with an exponential cut-off (Section 1.3).
The input parameters were chosen as follows:

- the reference radius R_0 is 1 AU (by default in the code);
- the power-law index p (SigmaSlope in Figure 3.2) has been put equal to 1;
- the cut-off radius $R_C = 45$ AU, not present in the original `.par` file, but added later. This value was initially taken from Dong et al. (2015a) (or Benisty et al. (2016)), that inferred it from the observations, so from the **actual** conditions of the disk. But this has already suffered the truncation process due to the companion star (Section 1.6), so there is the possibility that the value of R_C was higher at the disk formation. For this reason, some simulations were set with $R_C = 100$ AU as an initial condition.
- the reference surface density $\Sigma_0 = \Sigma(R_0)$, identified as Sigma0 in the `.par` file. This has been calculated through the following equation:

$$M_{disk} = \int_{R_{in}}^{R_{out}} 2\pi\Sigma r \, dr = \int_{R_{in}}^{R_{out}} 2\pi\Sigma_0 \left(\frac{r}{R_0}\right)^{-p} \exp\left(-\frac{r}{R_C}\right) dr \tag{3.23}$$

  where $R_{in} = 5$ AU and $R_{out} = 1000$ AU are the inner and the outer radius of the disk, and M_{disk} the disk mass.

This requires to know the parameter M_{disk}. Even this was adopted by Dong et al. (2015a), where $M_{disk} = 5 \cdot 10^{-3} M_\odot$. This value is obtained considering the total mass of the small dust grains to be $M_{small\,dust} = 5 \cdot 10^{-6} M_\odot$ multiplied by a factor of 1000 since it is assumed that the small dust grains contributes to 10% of the total dust mass, and considering a *gas-to-dust* mass ratio of 100:1. But again, this isn't

the mass of the disk at its initial configuration. To get this value, the calculation of the **cumulative mass** has been performed with an initial reference value for Σ_0, which was later multiplied for a certain factor to obtain the value of M_{disk} reported by Dong et al. (2015a). So the final value for the reference surface density results $\Sigma_0 = 2.17 \cdot 10^2\ g/cm^2$.

The other parameters set here are:

- the **aspect ratio** $h = H/r$ of the disk at the reference radius R_0, equal to 0.077. This was obtained using the value $H/r = 0.18$ at 30 AU and a trend of $H/r \propto r^{1/4}$, as suggested by Dong et al. (2015a).
  Even if the disk is simulated only in 2D, this parameter plays an important role in defining the initial condition of the sound speed c_s, since
  $$\frac{H}{r} = \frac{c_s}{v_K} \tag{3.24}$$
  where v_K is the Keplerian velocity;
- the **flaring index**, that was left equal to 0;
- the α**-viscosity** of the disk, which was put equal to $\alpha = 10^{-4}$ (Dong et al., 2015a), considering a Shakura-Sunyaev disk model (Section 1.3).

Planet parameters

The second set of parameters in the `.par` file regards the massive objects put in the mesh: stars and planetary companions. Their initial configuration is given in another file, the `.cfg` file, and an example of this can be seen in Figure 3.3. It contains the masses of the companions, expressed in units of the central star mass; their distance from the mesh center; and states whether these companions shall accrete their mass, and whether they feel the gravitational influence from the other companions in the same `.cfg` file.

Another important parameter shown in this section is the Eccentricity (e), which constrains the orbits of the objects in the file to be elliptical. The distance given in the `.cfg` file therefore becomes the *semi-major axis* a of the orbit, and the system is initialized such as the objects are at their *apoastron*, so at a distance equal to $a(1 + e)$.
Even if the considered disk is not on a face-on configuration (Section 2.2), the value of the Inclination parameter was left to 0, since the simulations were performed only in 2D.

Mesh parameters

The third set of parameters is referred to the working grid. The number of cells in each spatial direction is specified as Nx and Ny (and Nz in the 3D case). Immediately after, the limits for each direction are given. In the case of a cylindrical coordinates system, the X coordinate (representing φ) is periodic and its limits span from $-\pi$

to π; while along the Y coordinate (R) the minimum and the maximum radius are expressed through Ymin and Ymax.
For this last coordinate, a set of *ghost cells* is added: 3 of them under the minimum radius, and 3 above the maximum. These are used to set the **boundary conditions** of the problem (Section 3.3.2). These ghost cells are not necessary for periodic coordinates.

One more parameter that can be used is called Spacing: for cylindrical coordinates it sets the spacing step between two cells along the radial coordinate. Its default value is *linear*, meaning that the distance between two consecutive edges of the cells is given by

$$r_{i+1} - r_i = \frac{R_{max} - R_{min}}{N} \left(= \frac{\mathsf{Ymax} - \mathsf{Ymin}}{\mathsf{Ny}} \right) \tag{3.25}$$

otherwise it can be set to *log*, meaning that the space from a cell to the other equals

$$\frac{r_{i+1}}{r_i} = \left[\frac{R_{max}}{R_{min}}\right]^{\frac{1}{N}} \left(= \left[\frac{\mathsf{Ymax}}{\mathsf{Ymin}}\right]^{\frac{1}{\mathsf{Ny}}} \right) \tag{3.26}$$

This last grid type will be the one used in most of the simulations.
Moreover in this section it's possible to decide whether the reference system is fixed (*inertial*) or moving (*non-inertial*). The parameter Frame sets the type of the system, while OmegaFrame sets the angular velocity if the system is non-inertial.

Output control parameters

Apart from the output destination folder, this section is very important to establish the *time step* DT, which is the minimum temporal step between two **fine outputs** generated by the code. This value is also split in several elementary steps, and must be in agreement with the CFL condition (Section 3.2.2).
The Ntot parameter sets the total number of these time steps, setting also the total number of the fine outputs; while Ninterm sets the number of these steps after which a **coarse output** will be generated. These are the outputs from which the binary files will be created in the output folder, that can be converted in density maps, for example.

3.3.2 Other initialization conditions

Here are briefly summarized the other files in the `fargo` setup needed to initialize the configuration.

Boundary conditions (BCs)

The boundary conditions of a general problem are defined only for non-periodic coordinates in FARGO3D, so only for the radial one in the case of a 2D cylindrical set.
A series of files let the user to choose different BCs settings, using a certain number

of additional cells (along the non-periodic coordinates) in which they are applied, called *ghost cells*.
Without entering too much in the code details, the **keplerian BCs** were the one applied for the following simulations, for the density and the azimuthal velocity:

$$\Sigma_{gh} = \Sigma_{act}\left(\frac{R_{act}}{R_{gh}}\right)^{p} \tag{3.27}$$

$$v_{gh} = (v_{act} + \Omega \cdot R_{act})\sqrt{\frac{R_{act}}{R_{gh}}} - \Omega \cdot R_{gh} \tag{3.28}$$

where the subscripts *gh* and *act* corresponds to the *ghost* and the *active* cells, which are the cells of the mesh between Ymin and Ymax; p and Ω are respectively the parameters SigmaSlope and OmegaFrame in the `.par` file (see Section 3.3.1).

The .opt file

This is a file that allows to (de)activate different options or conditions, depending on the system or the problem the user wants to study. The most important between them are:

- **Coordinates system**: here the cartesian, the cylindrical or the spherical coordinate system has to be chosen. For the `fargo` setup, the cylindrical one is the only available.
- **Default star**: gives the possibility to remove the star in the center of the mesh, where it is located in the default configuration.
- **Potential**: (de)activates the calculation of the gravitational potential of the main star in the system $\phi = -GM_*/R$.
- **Viscosity**: (de)activates the calculation of the viscous tensor $\vec{T}$. Depending on the setting in the .par file, the viscosity ν (Nu) can be a constant, or can be calculated through the α-prescription (Eq. 1.9), if the Alpha parameter is specified.
- **Equation of state (EoS)**: sets the used EoS for the gas, that can be either *isothermal* or *adiabatic*. This choice changes the calculation of the initial speed sound c_s; the adopted case for the following simulations was the isothermal one:

  $$c_s = \frac{H}{r}\left(\frac{r}{R_0}\right)^{\beta}\sqrt{\frac{GM_\star}{r}} = \frac{H}{r}\left(\frac{r}{R_0}\right)^{\beta} v_K \tag{3.29}$$

  where β is the *flaring index* of the disk.
  Moreover, if the isothermal EoS is set, there is no need to calculate the energy equation from HD, since the internal energy of the system is constant;
- **Stockholm**: (de)activates the wave-killing Stockholm process near the boundaries of the mesh, in order to avoid the reflection of density waves on the borders that would generate unphysical effects. Even if it was always active, this parameter needed to be modified (see Section 3.4.2).

3.4 Graphics interpretation

3.4.1 Surface density images and profiles

The outputs of main interest are the **surface density images**, obtained both in *polar* and in *cartesian* coordinates, that allow a direct visualization of the structures that appear inside the disk; and the **azimuthal averaged surface density profiles**, that allow a more physical interpretation of the system during its evolution[4]. An example of the two representing the initial condition of some simulations can be seen in Figure 3.4.

The density images are obtained just assigning a color to every cell of the surface density array depending on its value, once the extremes of the used scale are fixed. This one is visible along the colorbar on the right of the 2D images, and for almost all the images it goes from $10^{-1}\, g/cm^2$ to almost $10^2\, g/cm^2$.
The images can be performed in *cartesian* coordinates or *polar* ones. These last ones will be particularly useful while modeling the spirals.
Regarding the profiles, let's consider an annulus at distance r from the center with wideness dr. The azimuthal average density profile is analytically expressed as

$$\overline{\Sigma}(r) \;=\; \frac{1}{2\pi}\int_0^{2\pi} \Sigma(r,\varphi)\, d\varphi \tag{3.30}$$

From a computational point of view, $\Sigma(r,\varphi)$ is given in arrays with $\mathsf{Nx} \times \mathsf{Ny}$ dimension, Nx and Ny being the number of cells in the azimuthal and in the radial direction respectively. So, for a fixed j cell along the radial coordinate, the azimuthal average density is computed as

$$\overline{\Sigma}_j \;=\; \frac{1}{\mathsf{Nx}}\sum_{i=0}^{\mathsf{Nx}} \Sigma(i,j) \tag{3.31}$$

Clearly, the higher the number of the cells, the higher will be the precision of this approximation compared to the analytical expression.

3.4.2 The Stockholm limit

Initially the simulations were run with a radial domain between $R_{min} = 5$ AU and $R_{max} = 1000$ AU. When only the companion star was put, the expected spirals and disk truncation (Section 4.1) did appear, but only beyond a certain radius (Figure 3.5 on the *left*).
However, the results of the simulations that included also the planetary companion didn't meet the expectations, since no cavity that could resemble the observations could be detected: the surface density didn't change in the proximity of the planet location, remaining quite identical to the initial condition. Only reducing the external radius of the mesh, the expected cavity started to appear. This is due to the presence, in the code, of a wave-killing formula by Val-Borro et al. (2006), which acts

[4]The presence of the grey area in this type of graphics is identified as **Stockholm limit** and it is explained in the Chapter 3.4.2

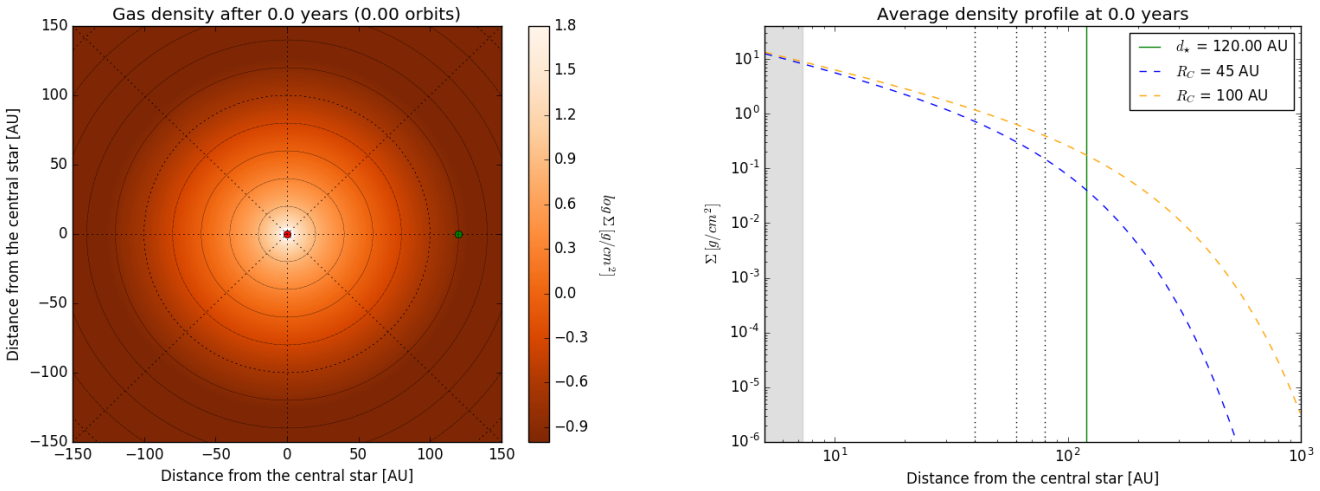

Figure 3.4: *Left:* Example of a **density image**, in cartesian coordinates, representing the initial conditions of a simulation expressed by Eq. 3.22, with $R_C = 45$ AU. The red and the green points refer to the main star (fixed) and the companion initial position, placed at 120 AU on the x-axis in cartesian coordinates (for a circular orbit). *Right:* Example of **azimuthal averaged density profile**, representing the same initial condition (in *blue*). The *orange dashed line* represents the initial condition for $R_C = 100$ AU. The *green solid line* shows the position of the dwarf companion star, while the *black dotted* ones are put as reference distances at 40, 60 and 80 AU.

in some intervals near to the radial domain limits. This approach is implemented to avoid the reflection of the density waves on the boundaries, that may significantly deviates the surface density values while the simulation is running.
By default, in the code the radius from which this wave damping is applied is calculated (on the inner border of the mesh) as

$$R_{inf} = R_{min} + 0.05\,(R_{max} - R_{min}) \tag{3.32}$$

which gives $R_{inf} \simeq 55$ AU for the values adopted. This means that all the density waves generated by gravitational perturbations of both the companions are drastically damped under this limit (Figure 3.5 on the *left*), giving unphysical results.
To solve this problem, but without deactivating the **Stockholm condition** in the `.opt` file, the R_{inf} value was recalculated as

$$R_{inf} = R_{min} + \log_{10}\left(\frac{R_{max}}{R_{min}}\right) \tag{3.33}$$

and reduced at $\simeq 7.3$ AU. This is under the nearest initial position performed for the planetary companion (8 AU).
Later on, this limit was also applied on the simulations with the companion star only, where at the beginning only the extremes of the spirals were visible. The application of Equation 3.33 drastically changes their configuration, since after that the spirals almost depart from the center of the mesh (Figure 3.5 on the *right*).

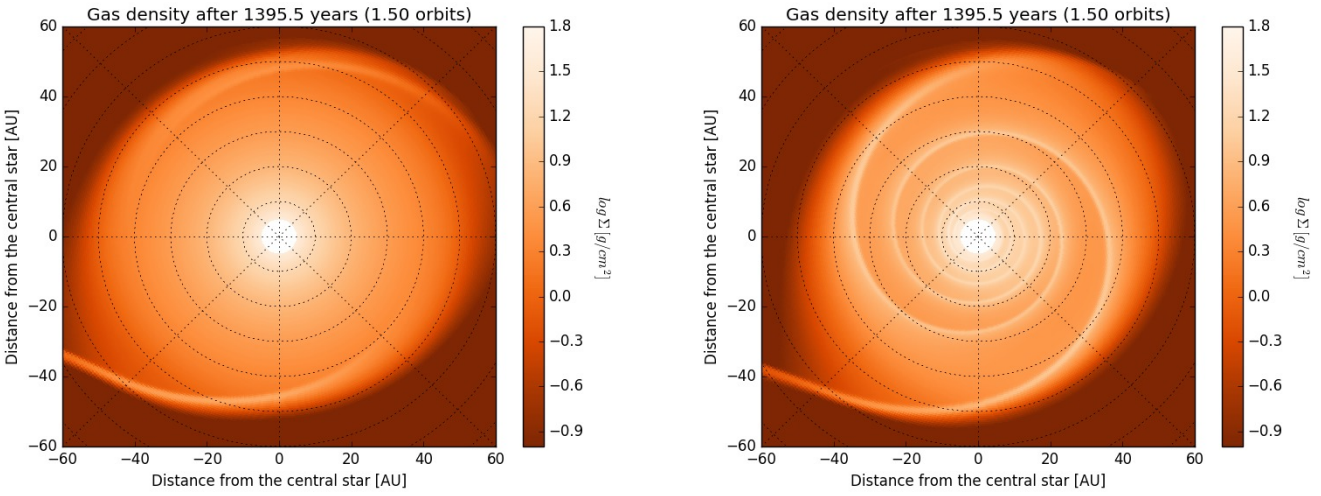

Figure 3.5: Outputs of a density image with the dwarf companion only, obtained without modifying the Stockholm condition (*left*), and after doing it (*right*). Only the very external parts of the spirals appear before calculating R_{inf} as in Eq. 3.33.

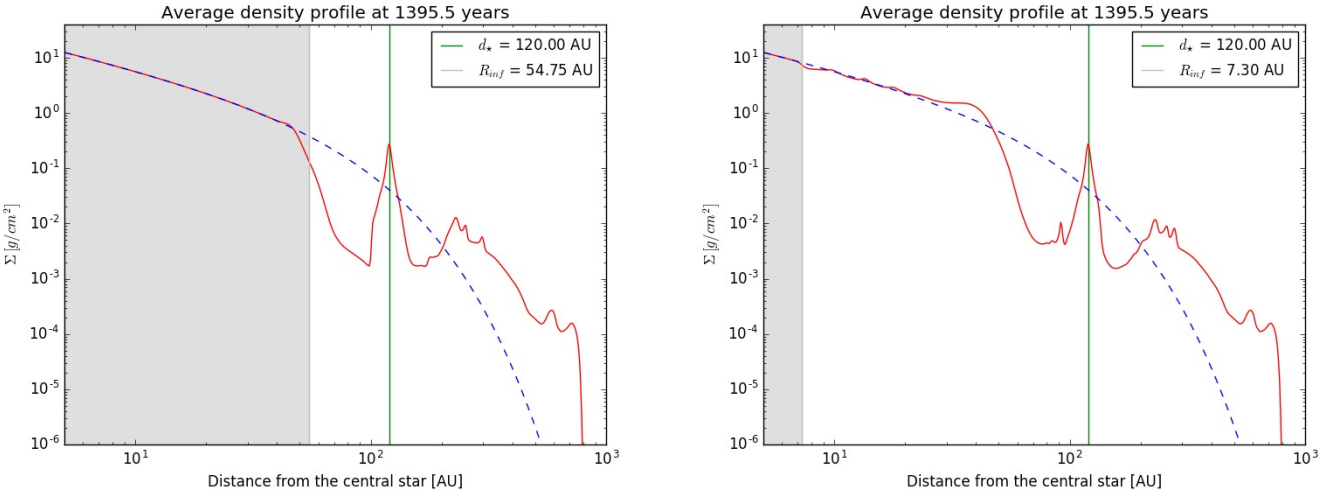

Figure 3.6: Outputs of a density profile with the dwarf companion only, obtained without modifying the Stockholm condition (*left*), and after doing it (*right*). The *grey area*, where the damping process is applied by the code, is drastically reduced when R_{inf} is calculated as in Eq. 3.33. Because of this damping, the averaged density profile strictly follows the initial condition under R_{inf}.

In all the density profile and cavity wideness graphics in the Chapter 4, a *grey region* will be present on the left border. This will have the same meaning it has in Figure 3.6: it represents the inner domain, from 5 AU to R_{inf}, in which the wave damping by Val-Borro et al. (2006) is applied by the code. Then the surface density values inside this area must not be considered realistic for this reason.

Chapter 4

Reproduction of the spiral arms and of the inner cavity

4.1 Simulations with the dwarf star only: reproducing the spiral arms

The first purpose for this thesis work was to try to reproduce the **double spiral arm pattern** observed in the HD100453 disk (Figure 2.1), considering the gravitational perturbations of the dwarf companion HD100453 B as the main responsible for their formation and sustaining.
As a first try, the orbit of the dwarf companion around the main star has been considered circular, and the orbit plane coincides with the disk one. This last one can be considered a good approximation: from the results of Wagner et al. (2018), that tried to constrain the orbital parameters of the dwarf companion, it results that its inclination is $i = 32.5° \pm 6.5°$, while the disk one is $\sim 28°$ (both counting from the line of sight). From the same study, also an eccentricity of $e = 0.17 \pm 0.07$ has been found. So, a second set of simulations with this value of eccentricity has been performed, to see what could be the differences in the triggering/maintaining mechanisms and in the properties of the spiral arms; and to see whether there is any variation in the disk truncation (Section 4.1.3).

4.1.1 Running time of the simulations

Before looking at the obtained results from the simulations, let's first resume some of the parameters used to run them.
The dwarf companion has been placed at a distance $d = 120$ AU, initially in a circular orbit around the main star. From the third Kepler's law[1], it's possible to

[1]Since the mass of the companion isn't negligible compared to the main star, it is necessary to consider it in the calculation of the orbital period.

find the orbital time:

$$T = 2\pi \sqrt{\frac{d^3}{G(M_A + M_B)}} \tag{4.1}$$

that corresponds to 930.4 yr, being the mass of HD100453 A and B respectively equal to $M_A = 1.7\,M_\odot$ and $M_B = 0.3\,M_\odot$. This is slightly bigger than the one estimated by Wagner et al. (2015) which is $\sim$ 850 yr. This can be a proof of the fact that the orbit is eccentric or that another massive companion could be present in the disk, which can influence the orbital period of the dwarf star.
Anyway, the parameters regarding the elementary step DT and the number of total outputs Ntot are based on the estimation from Equation 4.1. They have been adapted such as an orbit of the dwarf companion is complete after 100 outputs. Almost all the simulations were run for a time corresponding to 40 periods of the companion, which corresponds to about $3.7 \cdot 10^4$ years.
A second set of simulations has been performed with a companion star of 0.2 $M_\odot$ (value reported by Wagner et al. (2018)), but maintaining the same elementary temporal step. Since the total mass $M_{tot} = M_A + M_B$ is now lower, and since $T \propto (M_{tot})^{-1/2}$, the star will be slower in tracing its orbit, and at the end of the simulations it will complete one less orbit.

4.1.2 The disk truncation and the formation of the spiral arms

Let's have a look at the time evolution of the system. This is shown in the Figures 4.1 and 4.2, where on the *left* and *center* there are the 2-dimensional density images and on the *right* the respective azimuthal averaged surface density profiles, for the case where the **orbit** of the dwarf star is **circular**.
In the first image are represented some phases of the first orbit of the companion, in the second it's represented the situation after 2, 3, 5 and 10 orbits.
Both the **truncation of the disk** and the **formation of the spiral arms** are clearly visible already after the first few orbits of the companion, and the system gets in an almost stationary state just after about 10 companion orbits, like in Dong et al. (2015a) work. While the companion star runs its first orbits, the size of the disk starts to get well defined: a lot of material is pushed away because of the gravitational torques it produces on it, and a sort of "gas bridge" structure between the disk and the companion forms in the very first orbits. Some of this material is gravitationally captured by the companion, and starts to form a small gas disk even around it. The "bridge" structure tends to disappear after 5-6 orbits, reappearing only if some shocks are induced later (but always for a very short time, less than an orbit). Its remnant will be the main spiral arm of the disk, the one that points the companion.
The gaseous disk evolution can be seen in the density profiles[2]:

- at about 40 AU there is a little maximum in the density, after which there is a very steep decrease until it reaches a minimum at about 80 AU after

[2]The initial profile is the one with the cut-off radius $R_C = 45$ AU.

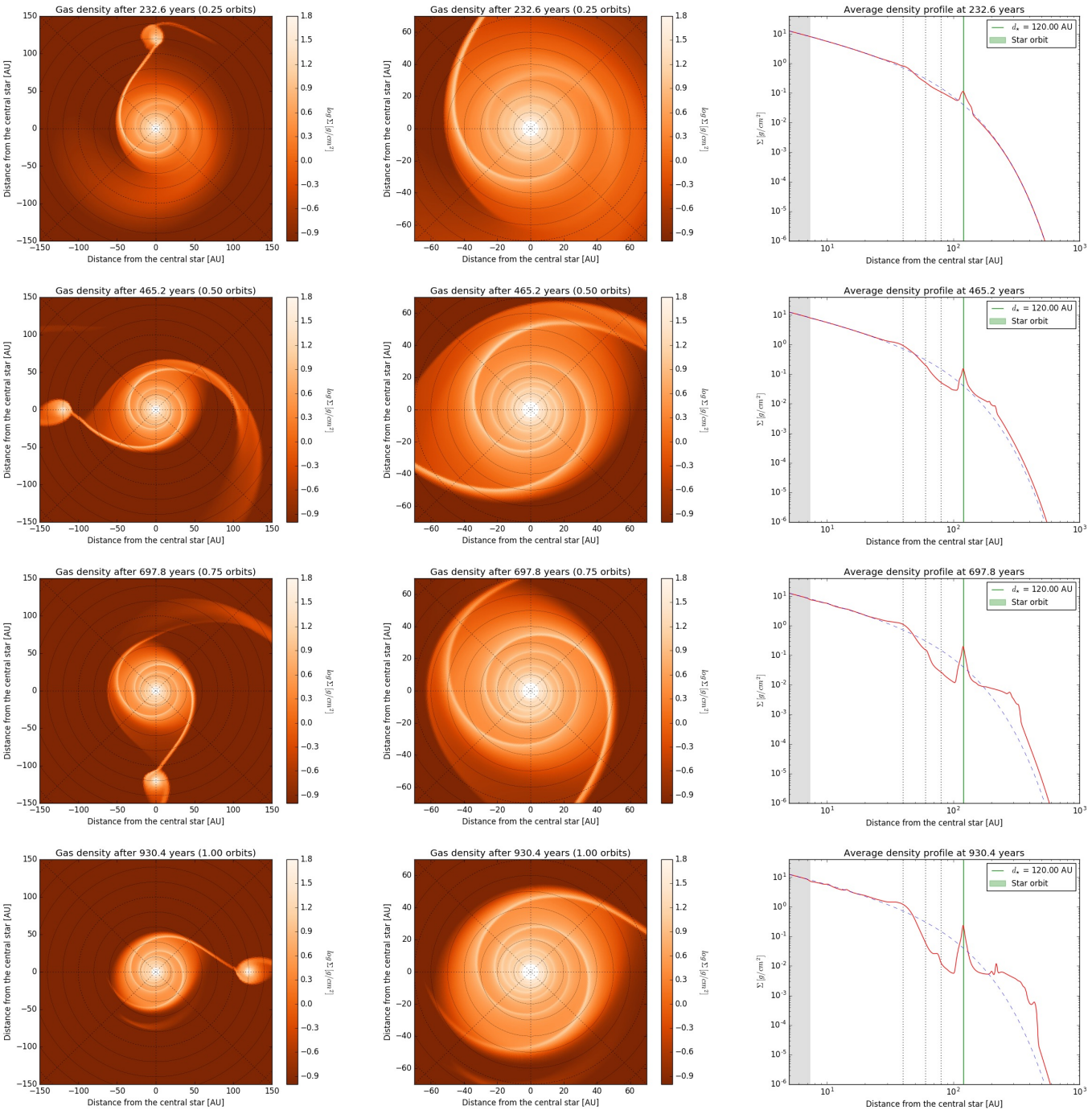

Figure 4.1: Simulation of the early evolution of the HD100453 system. The *rows* represent the evolution at 1/4, 1/2, 3/4 and 1 orbit of the companion (0.3 $M_\odot$) around the main star, in a circular orbit. In the *left column* it is possible to see the system until a distance of 150 AU, the *central column* is the same image zoomed at 70 AU to better look at the spiral structure and at the truncation of the disk. On the *right column* there are the respective azimuthal averaged density profiles, represented by the *red solid line*, in comparison with the initial condition (*blue dashed line*). The *black dotted lines* are put at reference distances of 40, 60 and 80 AU.

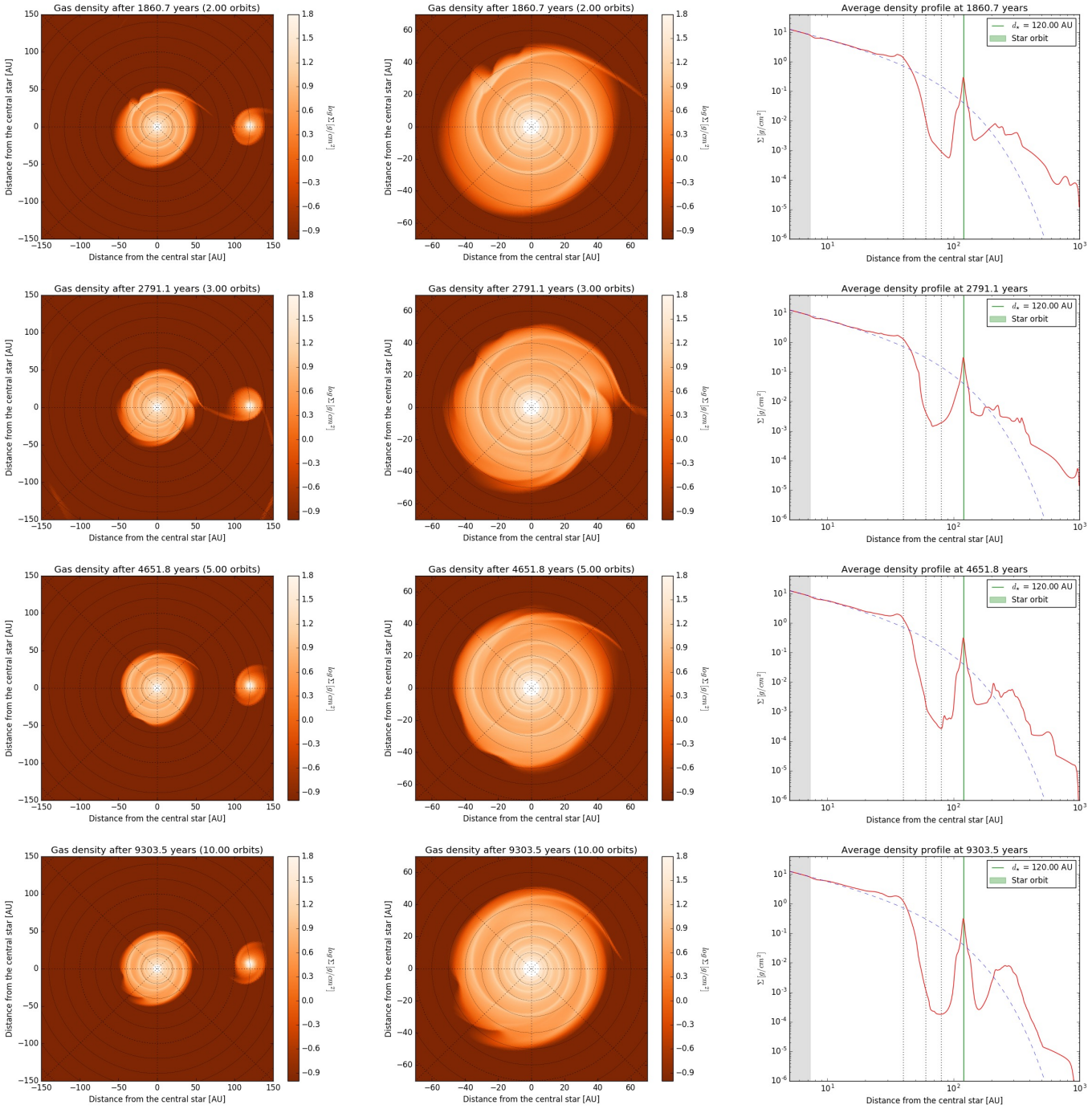

Figure 4.2: Simulation of the early evolution of the HD100453 system. The *rows* represent the evolution at 2, 3, 5 and 10 orbits of the companion ($M_\odot$) around the main star, in a circular orbit. In the *left column* it is possible to see the system until a distance of 150 AU, the *central column* is the same image zoomed at 70 AU to better look at the spiral structure and at the truncation of the disk. On the *right column* there are the respective azimuthal averaged density profiles, represented by the *red solid line*, in comparison with the initial density condition (*blue dashed line*). The *black dotted lines* are put at reference distances of 40, 60 and 80 AU.

10 orbits, much lower than the initial condition value (the *blue dashed line*). This minimum differs by about 4 orders of magnitude from the previous peak, from more than 1 g/cm^2 to $\sim 10^{-4} g/cm^2$. Both these values don't change significantly after 10 orbits.

- Beyond 80-90 AU the density profiles arises again very steeply, because of the presence of the companion star. But this peak extends for several AU: the gas is captured near the dwarf, and a small accreting disk is created around it, with a radius of about 20 AU. Interestingly, also in this disk it's possible to see a double spiral arm pattern, even if much weaker than the one in the main disk. One arm is a residual of the initial gas "bridge" structure and points to the main star of the system.

- Beyond this small disk structure the density profile reaches again a minimum to rise again above the initial condition after 200-300 AU. This situation is maintained until the end of the simulation and means that the companion pushed away some of the gas to the very external zones, until about 1000 AU.

The truncation radius

The **truncation radius** R_T can be qualitatively considered as the radius after which the averaged surface density assumes values lower than the one at its initial condition, in the range where it suddenly drops after the peak at about 40 AU. Looking at the final output (Figure 4.3, on the *bottom left*), R_T is placed at 41 AU. This value is more or less the same that has been reached just after 10 orbits, so just after $\sim 10^4$ years, considering an orbital period of 930.4 yr for a $0.3 M_\odot$ companion (Section 4.1.1). It is a very short time, compared to the typical lifetime of a protoplanetary disk, which is of the order of 10^7 yr.
The value of R_T is estimated on density profiles averaged along the azimuthal coordinate φ. Looking more in general at $\Sigma(r, \varphi)$, the disk looks a bit elongated in proximity of the spiral arms, especially along the one pointing the companion.
Let's compare this with the truncation radius obtainable from the criterion expressed in Section 1.6. According to the values reported in Tbable 1.1, this would result $0.40\, d < R_T < 0.47\, d$, considering a circular orbit of the companion and a value of μ equal

$$\mu = \frac{M_B}{M_A + M_B} = \frac{1.7\, M_\odot}{(1.7 + 0.3) M_\odot} = 0.15 \tag{4.2}$$

This means values of R_T between 48 AU and 56.4 AU, that are slightly higher than the ones obtained with the simulations: for these radii, the surface density drop already took place, with values that can be already under $10^{-2} g/cm^2$ (see Figure 4.2).

In the next Figure (4.3) there is a comparison between the outputs after 10 and 40 orbits of the companion, for two different initial conditions of the surface density. The equation for it (3.22) is the same for the two cases, but in the first one the cut-off radius R_C is equal to 45 AU (images on the *left*), in the second $R_C = 100$ AU (on the *right*). This last simulation has been performed to look at any differences in the truncation process if the external disk is more massive at beginning.

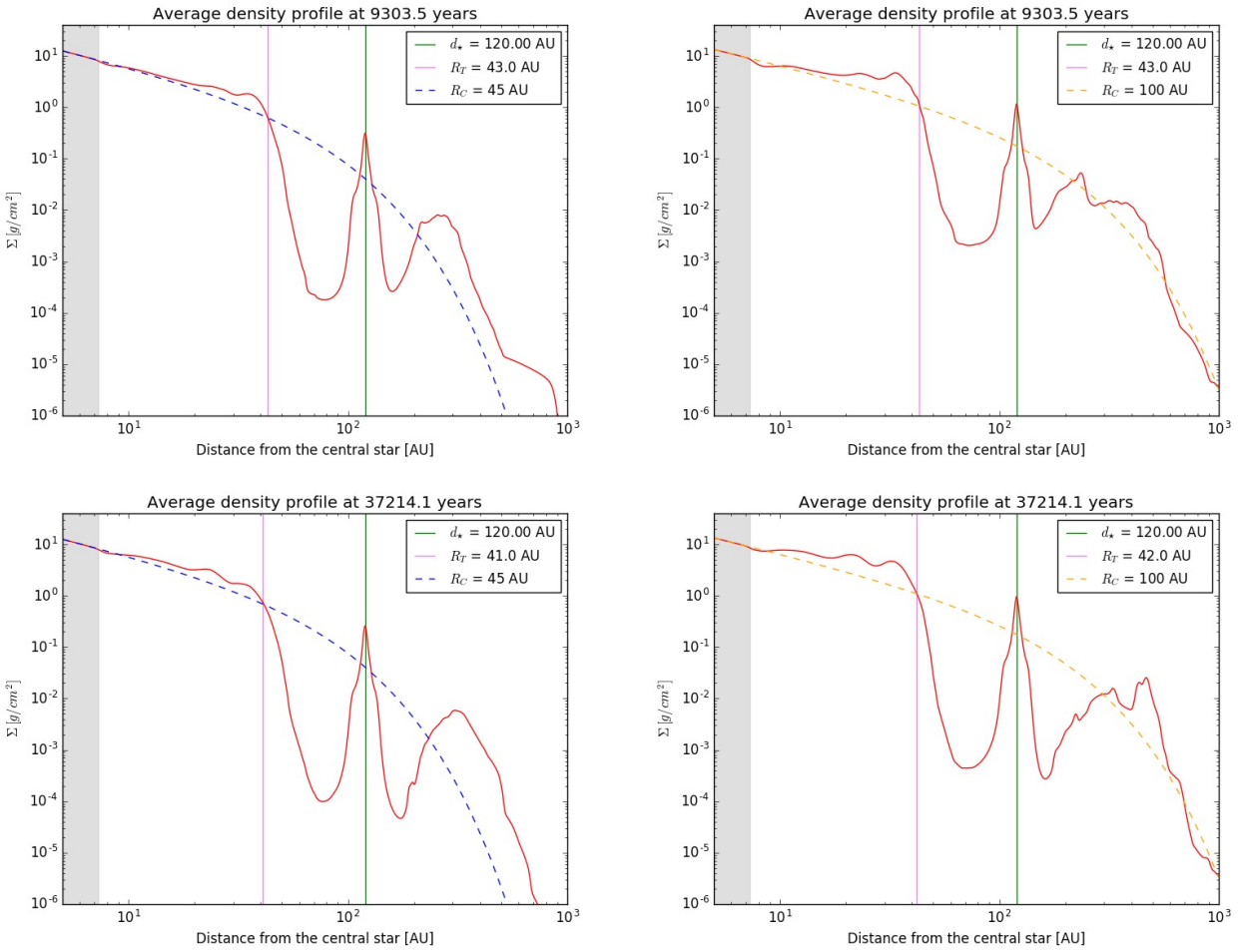

Figure 4.3: *Upper row*: azimuthal averaged surface density after 10 orbits of the companion (0.3 $M_\odot$), with a cut-off radius $R_C = 45$ AU on the *left* and $R_C = 100$ AU on the *right* in the initial condition (Eq. 3.22). The *violet solid line* shows the position of the truncation radius R_T. *Bottom row*: same as before, but after 40 orbits of the companion, at the end of the simulations.

The drop of the density verifies in both cases at about 35-38 AU both after 10 orbits and at the end of the simulations. This means that the truncation of the circumstellar disk happens in a very short time independently on the initial density profile[3], and even the value of R_T is very similar.
As expected, the density appears higher in the second case, both in the peak before the drop and in the minimum beyond 60 AU (about $2{\cdot}10^{-3} g/cm^2$ when $R_C = 100$ AU against $2 \cdot 10^{-4} g/cm^2$ when $R_C = 45$ AU, after 10 orbits). This difference is reduced at the end of the simulations, where the values of the minimum are respectively $\sim 5 \cdot 10^{-4} g/cm^2$ and $10^{-4} g/cm^2$.

[3]This is assumed to be valid until the disk mass is low enough to avoid self-gravitating effects ($M_{disk} \leq 0.1\, M_*$).

The formation of the spiral arms

The spiral arms start to form immediately from the beginning. Even if in the simulations only the **gas motion** is traced, while the **dust scattered light** is what is really observed, the main structure is reproduced: two spiral arms appear in an almost symmetric configuration (angle separation of about 180°). Their rotation is synchronous with the companion one, and their development direction is clockwise, contrary to the counterclockwise orbit of the dwarf star (Wagner et al., 2018).
One of the arms points directly to the companion, and it is stronger in intensity, as the SW arm observed in the system (Benisty et al., 2016). From the simulations, it also appears more extended than the other one (NE), contrary to the observations (Table 2.1). Another problem is that both the spirals are much more wrapped than what appears in the observations (see Section 4.1.4 for further details).

Shocks

In addition, it is possible to notice that some shocks are induced through the disk: these temporarily modify the structure of the spirals, which can partially broke (Figure 4.2, images referring to 2 and 3 orbits). These perturbations tend to stabilize after some time, and the spirals return to their previous shape without relevant changes on long term. The later the shock appears, the less will be its effect on the spiral arms; they just temporarily modify the shape of the external border of the disk, producing a more rosed-like shape.

Long-term effects

Since the simulations were run for about 40 orbits of the companion, any very long term effect can't be predicted in this thesis work. The time covered is of $\sim 4 \cdot 10^4$ yr, almost three orders of magnitude below the typical lifetime of a disk. A further improvement can cover more orbits of the companion, giving the possibility to investigate on long term effects that may emerge, such as further truncations, the onset of important instabilities/shocks or a non negligible eccentricity of the disk.

4.1.3 Eccentric orbit of the companion

Until now only a circular orbit of the companion star has been considered. Let's see what happens when this is instead **eccentric**, with $e = 0.17$ (value adopted from Wagner et al. (2018)), and maintaining the previous distance (120 AU) as the semimajor axis a of the new orbit. This means that its distance from the main star oscillates between $a(1+e)$ at the *apoastron* (where the simulation is initialized) and $a(1-e)$ at the *periastron*, which are respectively 140.4 AU and 99.6 AU.
The main difference lies in the behavior of the spirals, since their aspect strongly depends on the position of the companion star:

- after the apoastron (Figure 4.4 on the *left*) the spirals gets really weak, almost blending with the disk;

- after the periastron (Figure 4.4 on the *right*) instead, the spirals get much more evident and intense, more than the case without eccentricity.

During all the other phases of the companion orbit, the spirals are in a midway configuration between these two, that verify not at the exact correspondence of the apoastron and periastron passage, but about 0.2 periods later.
Also the extension of the spirals is similar, and the arm pointing the companion is more extended than the other one. Both the arms are more dense after the periastron, and their modeling has been applied at their maximum visibility.

In comparison with the circular orbit case, it is also possible to see that there are no substantial differences regarding the truncation radius, which always lies at 40-45 AU. The calculations performed by Artymowicz and Lubow (1994) expressed in Section 1.6 would give a truncation radius value of about 0.25 a, considering an eccentric orbit with $e = 0.2$ and $\mu = 0.15$, and a value of $\alpha = 10^{-4}$ in the α-viscosity prescription (Table 1.1). This means that $R_T \simeq 30$ AU, which is lower than the one found qualitatively in the simulations.

4.1.4 Modeling the spiral arms

Looking at the surface density images in polar coordinates, the spirals that are generated through the hydrodynamical simulations appear as *straight lines*, except for their extremes. Since there the radius is in logarithmic units, and the azimuthal angle φ in linear, this means that the spirals can be pretty well fitted through a **logarithmic spiral**, which general equation in polar coordinates is

$$r(\varphi) = a\, e^{b\varphi} \quad \Rightarrow \quad \ln(r) = \ln(a) + b\,\varphi \tag{4.3}$$

The second one appears as the equation of a straight line in the plane $(\varphi, ln(r))$.
A single equation has been considered valid for the parametrization of both the spiral arms, independently on their extension and intensity. The parameters a and b are summarized in the Table 4.1, for both the masses and the eccentricities of the companion.
Considering a reference system corotating with the companion and a circular orbit, the spirals are almost stable in intensity and shape (except when they are involved in some shocks), and a single evaluation of the parameters a and b is needed.
When instead the orbit is eccentric, the aspect of the spirals strictly depends on the position of the companion, so the parameters a and b are referred only to the configuration when they have the maximum luminosity and extension. This verifies about 0.2 orbits after the passage at the periastron.

	$e = 0$			$e = 0.17$		
	a	b	ψ	a_{per}	b_{per}	ψ
0.2 $M_\odot$	1.0	0.108	6.1°	1.0	0.109	6.2°
0.3 $M_\odot$	1.0	0.114	6.5°	1.0	0.120	6.9°

Table 4.1: Parameters for the fitted logarithmic spirals.

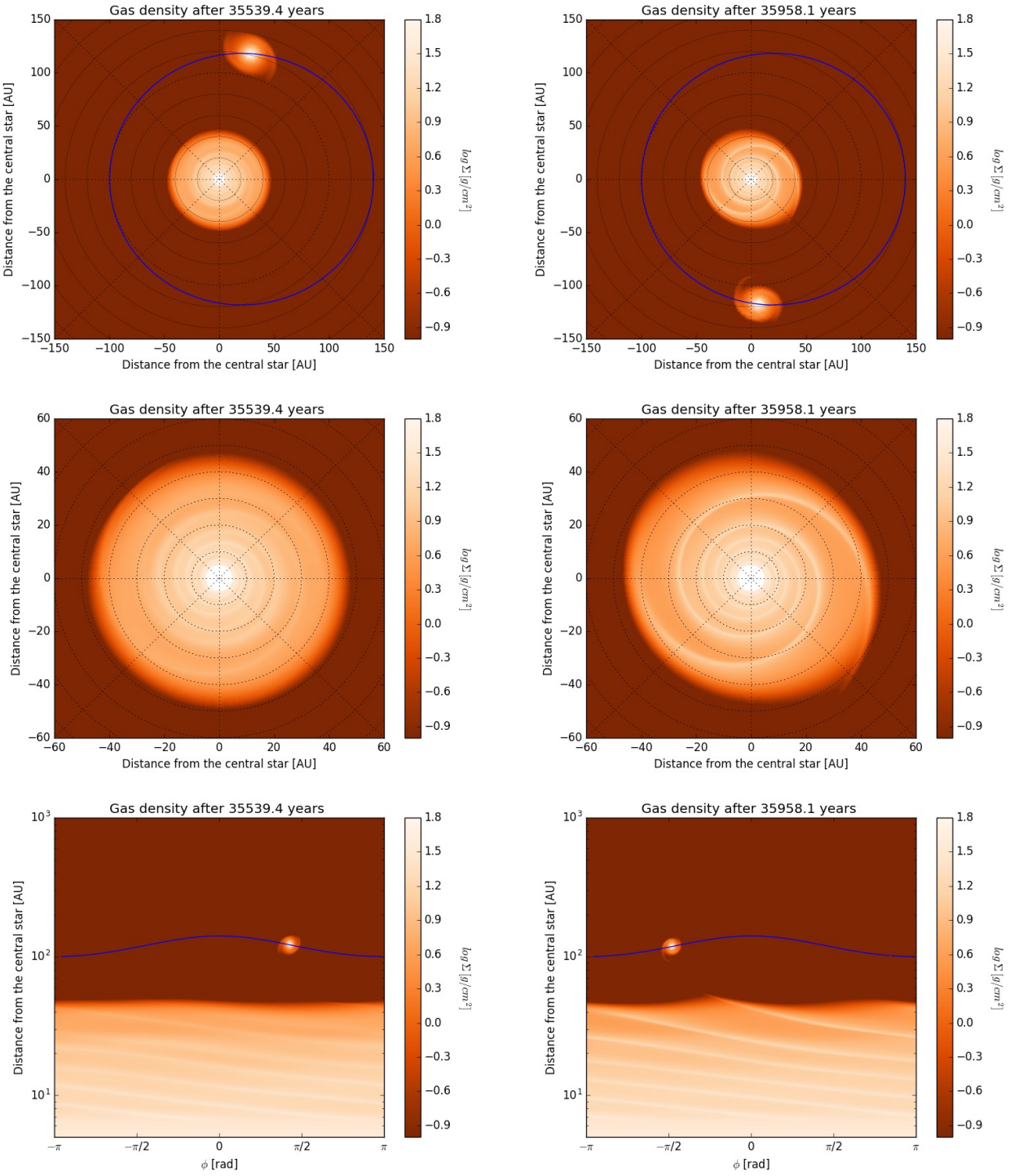

Figure 4.4: Spiral arms behavior for a 0.2 $M_\odot$ companion with eccentricity $e = 0.17$. The orbit is represented by the *blue solid line* and it's counterclockwise. So the images on the *left* show the situation after ~ 0.2 periods after the passage at the **apoastron**; on the *right* the same after the **periastron**. The images on the *central row* are just zoom of the *upper row* 2D images, while the *bottom row* show the same images in polar coordinates.

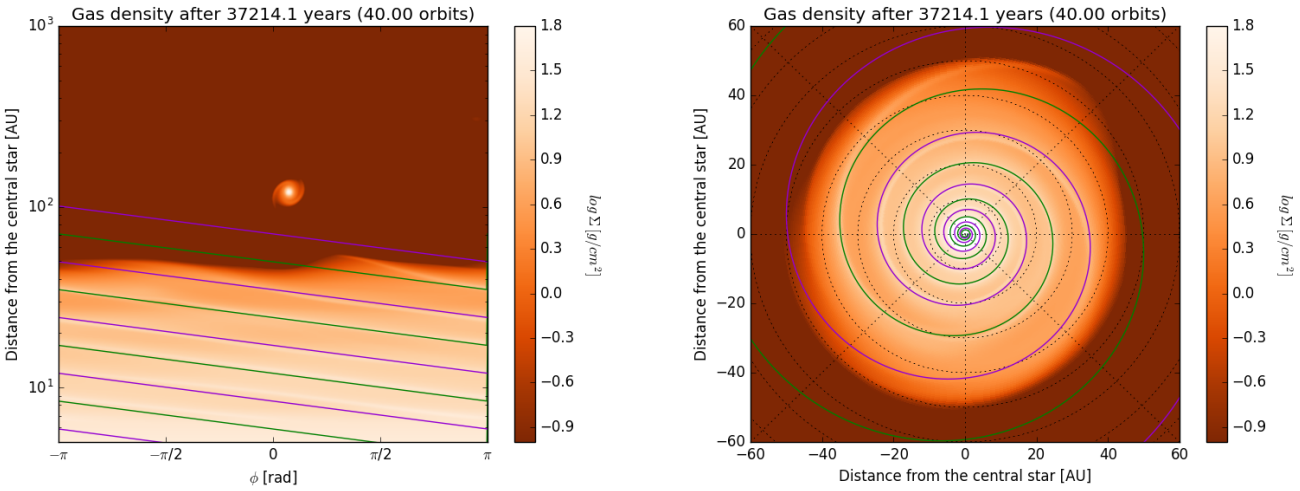

Figure 4.5: Fitting of the spiral arms for a 0.3 $M_\odot$ companion with circular orbit, in polar coordinates on the *left* and cartesian on the *right*. It's clear to see how they appear as straight lines in the polar projection.

Finally, looking at the different mass of the companion, the spirals appear to be a bit more open when this is more massive (increase of the parameter b), and also the eccentricity seems to play a more significant role in this case.

After that, the **pitch angle** of the spirals has been calculated: given a circumference (centered in the spiral pole) that intersects the spiral, this is defined as the angle between the tangent lines of the two curves in the intersection point. Thanks to the properties of the logarithmic spiral, this angle is always the same, independently on the position of this point. Considering that

$$\frac{dr(\varphi)}{d\varphi} = a\,b\,e^{b\varphi} = b\,r(\varphi) \tag{4.4}$$

the **pitch angle** ψ is equal to

$$\psi = \frac{\pi}{2} - \tan^{-1}\left(\frac{r}{\frac{dr}{d\varphi}}\right) = \frac{\pi}{2} - \tan^{-1}\left(\frac{r}{br}\right) = \frac{\pi}{2} - \tan^{-1}\left(\frac{1}{b}\right) \tag{4.5}$$

The values of ψ are reported for each value of b found, in the Table 4.1. The angles that result are lower than 7°, much different from the ones observed of 38° for the weakest arm (NE) and of 30° for the strongest one (SW) (Benisty et al., 2016). There are no substantial differences in the values of ψ with the mass and the eccentricity of the companion, so there must be some other considerations to do:

- first of all, the inclination of the disk ($\sim 28°$, from Wagner et al. (2018)) would have no negligible projection effects. However, this consideration would further reduce the pitch angles that have been found, and seems not helpful to solve the problem.

- What is mapped in the simulation is the surface density of the gas, while what is observed (Figure 2.1) is the light scattered by the dust on the disk surface. There is the possibility that this doesn't strictly follow the gas motion, getting a different distribution.
- Even if the disk height has been set, no hypothesis have been done about **flaring**: this factor, combined with inclination, would change the projected view of the spirals, and consequently even the value of their pitch angle.

These considerations would be object of future improvements, using for example a radiative transfer calculation code, like RADMC-3D (Dullemond, 2010).

4.2 Simulations with the planetary companion: reproducing the inner cavity

As already mentioned, the disk of the HD100453 system presents a **cavity** in its inner part, where the signal from dust-scattered light is missing. This extends until about 16 AU (Section 2.2.3). The inner edge of this hole seems to be really close to the star, where another inner disk of dust seems to be present.
The companion dwarf, as can be seen in the previous simulations, is not able to reproduce by itself the presence of this cavity: in the Figures from 4.1 to 4.5 it's clear that the spirals are present also under the limit of 16 AU, but this is not observed.
Another inner companion, probably **a planet or a brown dwarf**, is here assumed as the main responsible for the formation of this cavity in the system. A lot of previous simulations and works seem to confirm this trend, since a planet in a disk tends to clean its surrounding area, accreting itself or pushing away the material due to its gravitational interactions (Section 1.4.1).
Anyway, not every planet is able to produce such holes, typically only Jupiter-like planets (or even more massive ones) can do that (Paardekooper and Mellema, 2004). So the simulations have been performed only with planets with masses $M_P \geq 1\, M_J$.

The second aim of this thesis work is to reproduce the inner cavity of the HD100453 disk in order to characterize this planet companion inside the system, or to exclude possible candidates. This has been done looking in particular at its mass, its distance and the eccentricity of its orbit. Moreover it will be possible to characterize this planet looking at its influence on the structure (or at the presence) of the spiral arms generated by the companion star.

4.2.1 Planets sets

The simulations were performed with different sets of planets, with the following combined characteristics:

- **Distance:** three sets of distances where the orbit of the planet was initialized: 8, 10 and 12 AU. Some tests have been performed even at 15 AU.
- **Mass:** the chosen masses were 1, 3, 5, 7 and 10 M_J.

- **Eccentricity:** the simulations can also be divided in three groups looking at the eccentricity of the orbits of the planet and of the dwarf star: one considering no eccentricity for both, one only for the star, and one for both the companions. The eccentricity is always initialized with the value of 0.17, when it's present.

Finally, the sets have been applied twice, for the two values of the mass adopted for the companion dwarf (0.2 or 0.3 $M_{\odot}$), for a total number of 90 simulations. These were run for the same number of time steps used for the simulations without the planet, but this total time period corresponds to slightly more than 40 orbits (in the case of 0.3 $M_{\odot}$) since the period of the companion star reduces, as much as more massive is the planet.

4.2.2 The inner cavity

The main effect of the planet on the disk is to clean it in its surrounding zones, accreting itself or pushing away the material. This can be seen in the following Figures (4.6-4.7-4.8), where three configurations are taken as examples, described in the respective captions. There are shown the 2D density images on the *left column* (limited at 60 AU from the center), and the azimuthal averaged surface density profiles in the *center* one, at different times of the simulations.
For the profiles, starting from the initial condition (*blue dashed line*), the planet is identified by the *pink solid line*, while the *pink area* is the wideness of its orbit. Of course, this is much more extended if its initial eccentricity is set equal to 0.17, as the stellar one. It is possible to see how the surface density around the planet gets lower with time, until reaching 2 or 3 orders of magnitude under the initial level at the end of the simulations (last row of every image). This means that the simulated planet can be considered as a good candidate for the formation of a hole in this system.

The amplitude of the cavity has been calculated considering the radius range in which, at a certain time, the azimuthal averaged surface density profile $\Sigma(t)$ is lower than the one at the initial condition Σ_0. This is shown in the *right column* of the Figures 4.6-4.7-4.8, where the x-axis is the radius, and the y-axis is the difference $\Sigma(t) - \Sigma_0$, represented by the *red solid line*. The *blue dashed* one represents the surface density initial condition (equation 3.22) normalized to 0; the *pink solid line* points out the position of the planet at that specific time, and the *pink area* shows the wideness of the cavity.

While the outer border of the cavity is often well defined, it's important to make a consideration about the inner one: in almost all the cases this is just a bit lower than the wave-killing boundary limit R_{inf} (except for some of the lowest mass planets), but this can't be considered a real value, as already said in Section 3.4.2. So, since in the images of the system (Figure 2.1) there is no evidence for an inner disk to be present, it's necessary for the inner border of the generated cavity to lie below R_{inf}. On the contrary, the planet is placed too far or is not massive enough to generate the observed hole[4].

[4]Some other effects, such as photoevaporation, can be responsible for the disk cleaning in the

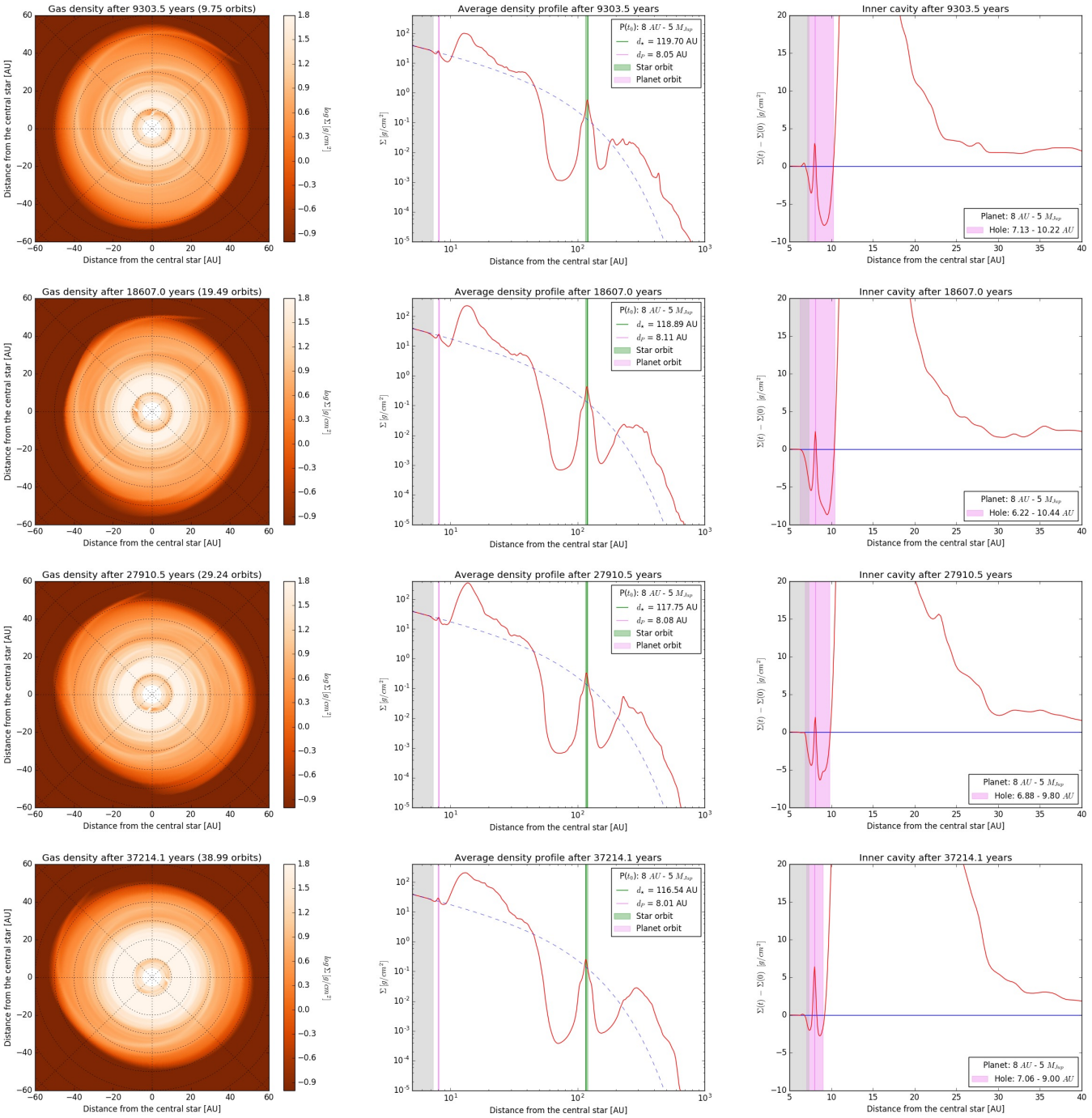

Figure 4.6: Surface density images (*left*), azimuthal averaged density profile (*center*) and extension of the cavity (*right*) at various times for a system with a 5 M_J planet at 8 AU and $e = 0$ for both the companions.

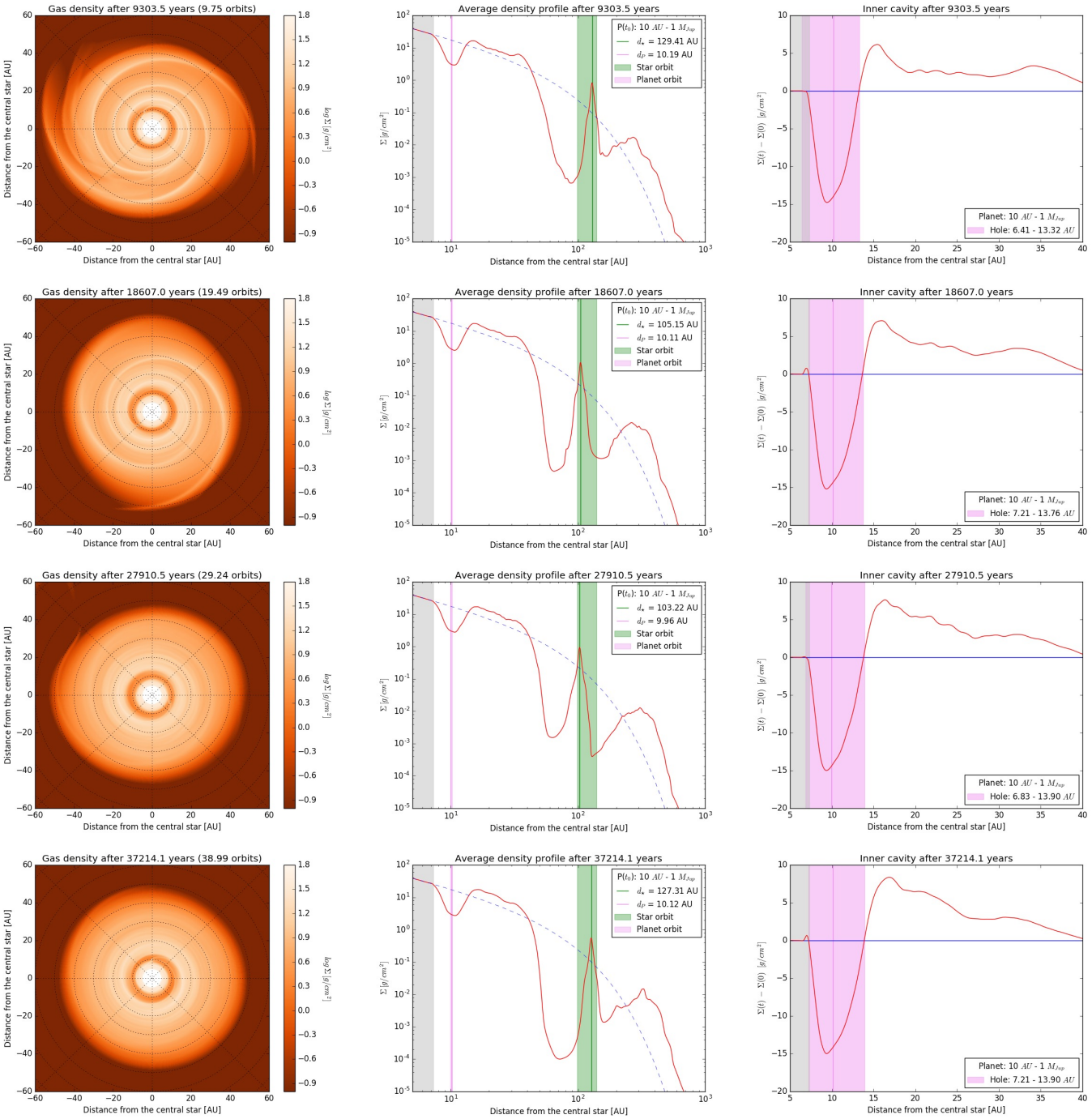

Figure 4.7: Surface density images (*left*), azimuthal averaged density profile (*center*) and extension of the cavity (*right*) at various times for a system with a 1 M_J planet at 10 AU and $e = 0.17$ only for the companion star.

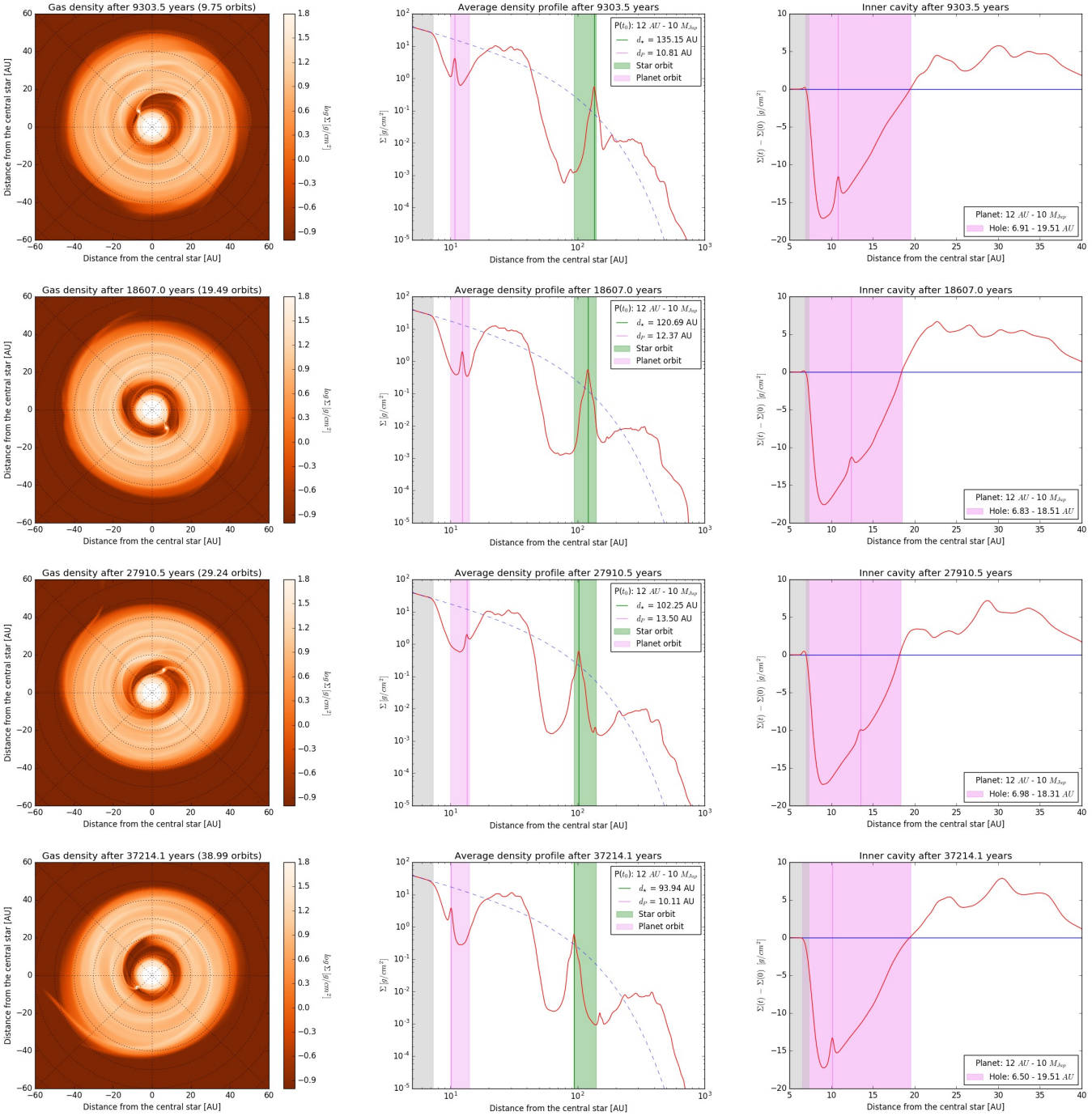

Figure 4.8: Surface density images (*left*), azimuthal averaged density profile (*center*) and extension of the cavity (*right*) at various times for a system with a 10 M_J planet at 12 AU and $e = 0.17$ for both the companions.

Star mass	0.2 $M_\odot$					0.3 $M_\odot$				
Planet mass	1 M_J	3 M_J	5 M_J	7 M_J	10 M_J	1 M_J	3 M_J	5 M_J	7 M_J	10 M_J
Distance	e = 0									
8 AU	9.59	9.90	9.00	10.22	10.55	9.39	9.90	10.12	10.44	10.33
10 AU	13.90	14.05	14.35	14.20	14.35	13.90	14.05	14.35	14.35	14.35
12 AU	16.30	18.51	19.51	19.10	19.10	16.13	18.12	19.10	19.10	19.10
15 AU	19.93	21.70	22.63	23.87	24.38	19.51	21.24	22.16	22.88	24.12
Distance	e = 0.17 (star only)									
8 AU	9.59	10.01	10.33	10.12	10.55	9.59	10.12	10.22	10.44	10.67
10 AU	13.90	14.20	14.35	14.50	14.50	13.90	14.05	14.50	14.66	14.35
12 AU	16.13	18.51	20.14	19.31	19.51	16.13	18.90	19.31	18.51	18.51
15 AU	19.51	22.63	23.87	24.38	23.87	19.10	22.63	23.37	23.12	24.12
Distance	e = 0.17 (both)									
8 AU	9.59	9.90	10.33	10.12	10.67	9.59	10.12	10.01	10.33	10.55
10 AU	14.66	14.50	13.90	14.20	14.50	14.50	14.81	13.61	14.50	14.05
12 AU	16.82	19.51	22.63	17.00	19.51	16.65	19.51	22.40	17.18	18.90
15 AU	19.93	22.88	24.90	20.58	23.87	19.10	22.40	24.64	23.12	24.12

Table 4.2: Values of R_H at the end of every simulation. The values on the *top* represent the mass of the companion star, while the ones immediately *lower* the mass of the planet put in the simulations. On the *left* there is the distance at which the planet is initialized. Note that for the last table, where $e = 0.17$ also for the planet, the distance must be multiplied by $(1 + e)$ to obtain the initial position.

To find which planet can better reproduce the wideness of the hole in the disk, the various configurations were analyzed considering different parameters. In the Table 4.2 are listed all the maximum radius of any cavity, which will be called R_H. This corresponds to the external radius of the hole at the last output of every simulation, at least for the ones where the initial eccentricity of the planet is set equal to 0. Instead, in the simulations where the eccentricity of the planet is 0.17, there will be an interval of values of R_H between subsequent outputs, since it changes as the planet is closer or farther from the central star. In this case, the reported value of R_H is an average of the values for the last 100 outputs of every simulation.

For a better visualization of the distribution of R_H it is possible to refer to the Figures 4.9-4.10, built for all the simulations with the companion star having a mass of 0.2 $M_\odot$ or 0.3 $M_\odot$.

inner AUs. This can be combined with a low mass planet to generate the observed cavity.

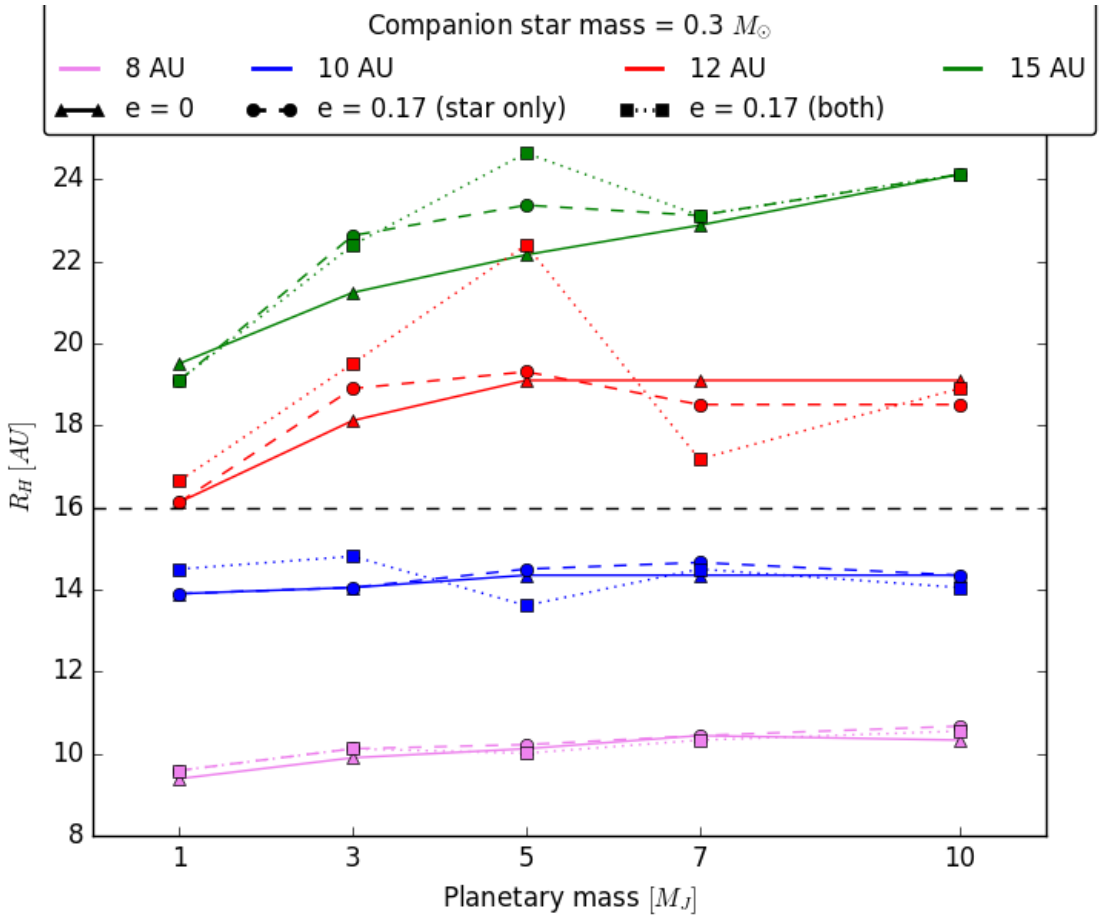

Figure 4.9: Values of R_H for all the simulations performed with a companion star of 0.3 $M_\odot$. Note that in the case of $e = 0.17$ for both the bodies, the *squares* are representative of the middle value of R_H, since it changes depending on the distance of the planet from the main star. The *black dashed line* at 16 AU points the maximum observed extension of the hole in the disk.

4.2.3 Characterization of the planet

Looking at the Figures 4.9-4.10 it is possible to make some considerations about the characteristics that the planet should have to generate the observed hole, which external observed radius is $\sim$ 16 AU (Benisty et al., 2016).
Unfortunately, no one of the simulations has been performed with the appropriate parameters to have a value of R_H really close to 16 AU. The cases with the planet with 1 M_J initially positioned at 12 AU (especially the ones with $e = 0$) seem to be good candidates to obtain a final external radius of the hole at 16 AU, but they fail in reproducing its inner border: looking at the Figure 4.11, it is possible to see that the *pink area*, representing the hole wideness, and the *grey area* (under the Stockholm limit) don't overlap, so it is possible to consider the inner radius of the generated hole as a realistic result of the simulation.
But as told in Section 4.2.2, the inner edge of the cavity is really close to the main star, much lower than the R_{inf} value, and a 1 M_J planet seems not able to generate

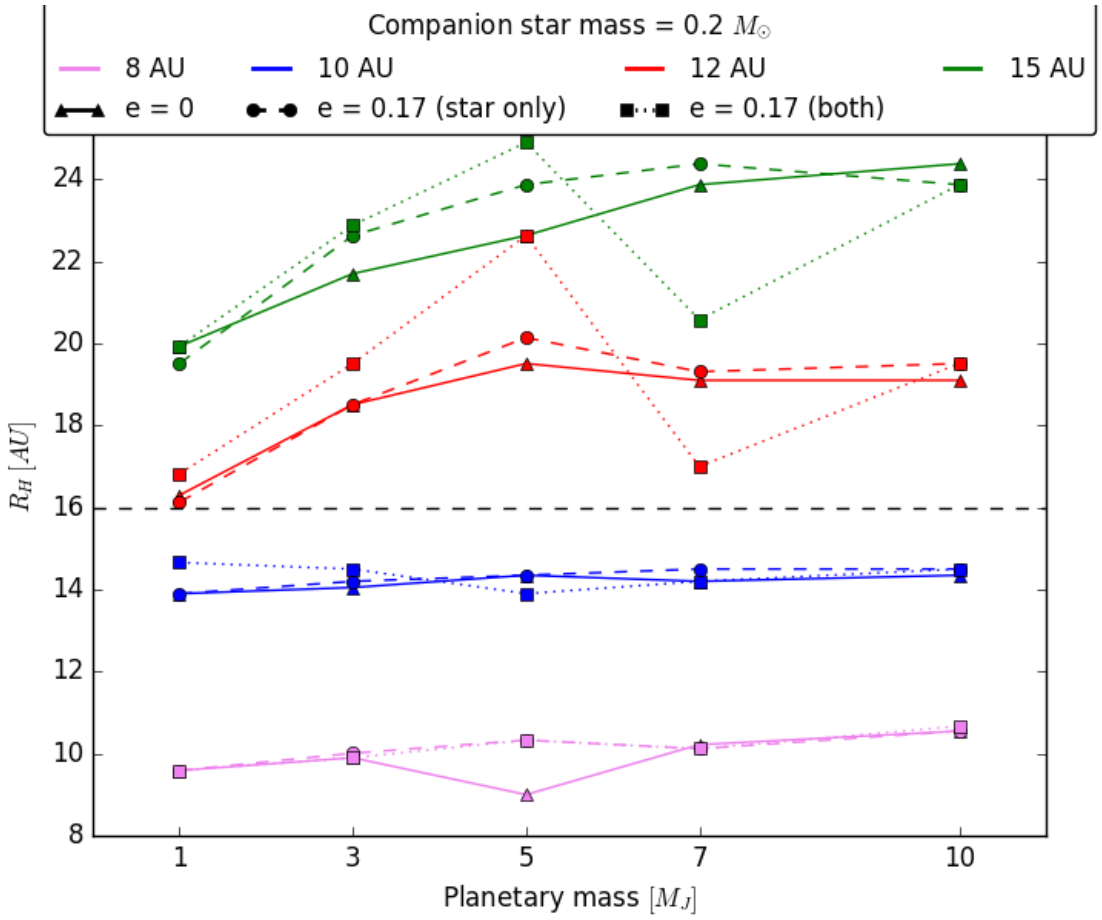

Figure 4.10: Values of R_H for all the simulations performed with a companion star of 0.2 $M_\odot$. Note that in the case of $e = 0.17$ for both the bodies, the *squares* are representative of the middle value of R_H, since this changes depending on the distance of the planet from the main star. The *black dashed line* at 16 AU points the maximum observed extension of the hole in the disk.

a so wide cavity, at this distance. So these planets can't be considered as good candidates for the generation of the observed hole (or they have to be implemented with other physical phenomena). Only in the case of $e = 0.17$ for the planet, this condition is verified, but looking at the results of the cases with $e = 0$, it's improbable that the inner edge can almost reach the main star.
On the other hand, planets with the same initial distance and higher mass generate wider cavities, with R_H of about 18-19 AU, where instead the main ringed-structure of the disk is clearly present (Benisty et al., 2016).
Looking at the planets initially positioned at 10 AU, it is possible to see that in any case it isn't possible for R_H to reach the observed value, since it arrives until only 15 AU. Also there seem to be not so much dependence on the mass of the planet, or on its eccentricity, as in the case of the planet positioned at 12 AU (see Section 4.2.4).
So probably, to obtain a cavity in the simulations that resembles the real observed one, a single planet should have an orbit with a radius in between, so at about 11

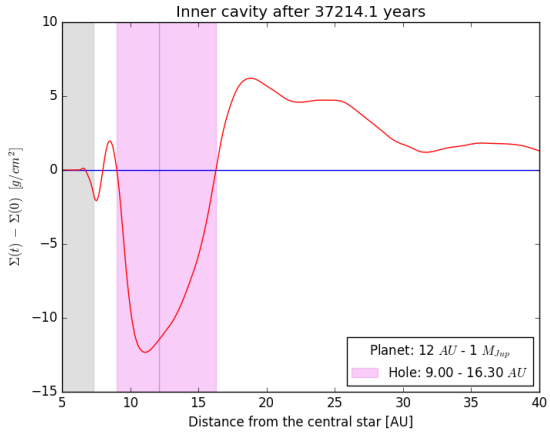

(a) $e = 0$

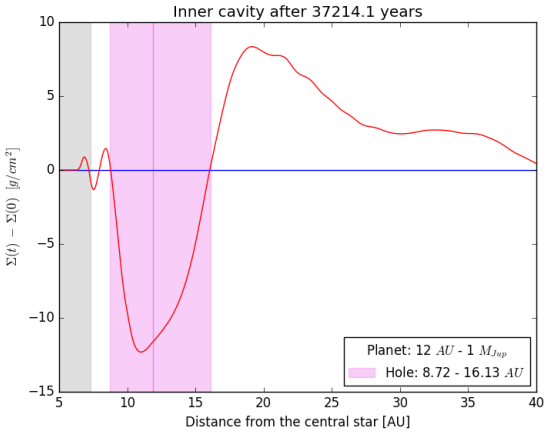

(b) $e = 0.17$ (star only)

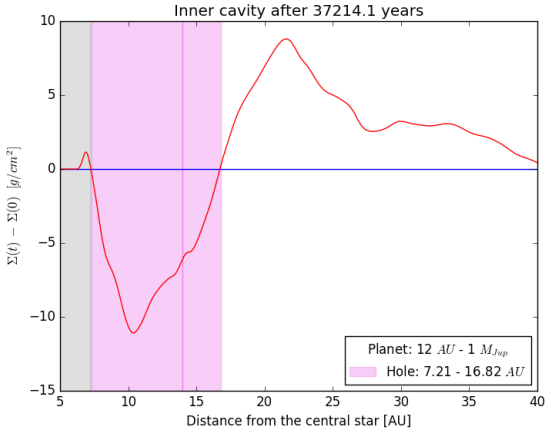

(c) $e = 0.17$ (both)

Figure 4.11: Last output for the simulations of a planet of 1 M_J initialized at 12 AU, with the three cases for the eccentricity (and a 0.2 $M_\odot$ companion star). It is possible to see that for the first two cases the inner radius of the cavity doesn't get a value lower than R_{inf}, while this happens for the last one.

AU; and its mass must be over 2-3 M_J to produce an enough large hole even on the internal side.

4.2.4 Dependences of R_H

Looking at the graphics in Figures 4.9 and 4.10, it is possible to analyze how the variations in the initial mass, distance and orbit eccentricity of the planet have their influence on the final value of R_H.
First of all, it must be considered that the values of R_H depend sensitively on the size of the grid and on the number of the cells. Since this is limited (500 cells on the radial coordinate) the precision can't be infinite, and that's also the reason why the values in the Table 4.2 can be repetitive.

Fixing the distance, it is possible to see that in general the external radius of the hole increases with the mass of the planet. This is quite intuitive since the more massive the planet, the farther will be the gas that feels its gravitational field, and that can accrete it or be pushed away. This trend, anyway, seems to have two different behaviors, depending on the initial distance at which the planet is:

- at 8 and 10 AU, the value of R_H is almost stable: it increases, but very slightly and only at low masses, of only about $0.5 - 1$ AU. In some cases it can also reduce, as for the case of the 5 M_J planet at 8 AU, without eccentricity and with a companion star mass of 0.2 $M_\odot$.

- at 12 and 15 AU, there is a rapid increase of R_H between 1 and 5 M_J, of about $2 - 3$ AU. For more massive planets, the values tend to stabilize or even to reduce for the planets at 12 AU, or to still increase slightly for the 15 AU case, especially if the planet orbit has no eccentricity. In the case where it is $e = 0.17$, the values of R_H are much more variable, and this may be a sign of incoming instabilities for massive planets at this distances, if their orbit isn't nearly circular. The values resemble more the ones obtained with $e = 0$ only for planets with 10 M_J.

This double trend can be due to the combined effect of the increasing influence of the gravitational field of the external companion star, and the decreasing one of the main star, as the position of the planet gets farther from the center of the system. In any case, the value assumed by R_H is mainly dependent on the initial distance of the planet, while the mass and the eccentricity of the system play a secondary role, especially for planets closer to the main star.
Finally, looking at the different mass of the companion star, it is possible to see from the values in the Table 4.2 that this has negligible influence on the variations of the values of R_H.

4.2.5 Effects of the planet on the spiral arms

Looking at the images in the Section 4.1, it's clear to see that the double spiral arm pattern reaches almost the inner edge of the mesh, without the formation of a cavity and their interruption at a distance of about 23 AU (Section 2.2.2, Benisty et al. (2016)), where they blend with the main ring structure, as can be seen in Figure 2.1. Moreover, in the observations the spirals are drastically interrupted by the shadows identified in the disk (Section 2.2.2), that aren't reproduced by the simulations, since no inner disk is performed. As already mentioned, there is no evidence to establish whether this is a coincidence or not.

In Figure 4.12 there is a comparison between the final outputs in a simulation with and without a planet, to see the differences that the second body could induce. The companion star mass is 0.2 $M_\odot$, while the planet one is 5 M_J and it is initialized at a distance of 12 AU, with the three different eccentricity conditions.
The formation of the inner hole and the interruption of the spirals is clear in all the

cases, but it's possible to see some differences about the effects on their shape and intensity:

- when $e = 0$ for both the bodies, the spiral shape is maintained almost wrapped as in the case without the planet, while they tend to be more opened when $e = 0.17$ for the star only and even more when also the planet orbit is eccentric.
- when $e = 0$ the intensity of the spiral arms is pretty similar (for radii bigger than R_H), while for the other cases their structure result much more evident, so their density is higher, even more when also the planet orbit is eccentric.
- the length of the spiral arms remains almost the same, reaching about 50 AU for the main arm. The only exception is when $e = 0$ for the planet orbit and $e = 0.17$ for the companion star, where this reduces at about 40 AU.

In Figure 4.13 it's possible, instead, to see the effects of planets of different mass on the spiral structure. With respect to the case without the planet, it can be seen that the spirals tends to get more wrapped as the planet mass increases. This is quite intuitive, since the more massive the planet, the stronger will be its gravitational attraction to it, and this tends to move the spirals more inside the disk. In the last case, where $M_P = 10\ M_J$, the spiral structure is almost completely lost, as it is too near to the main ring of the disk.
Following this approach, it is possible to say that, if a single planet is present in the HD100453 system, this can't have a mass of the order of 10 M_J, because it would modify the spiral arms generated by the companion in a way that doesn't match the observations.

Finally let's consider the different distances at which the planet is initialized in the simulations. Examples of a planet of 5 M_J and no eccentricity, initialized at 8, 10 and 12 AU are reported in Figure 4.14. It is clear to see that the closer is the planet to the central star, the more undefined will be the spiral structure. Moreover, the surface density seems to be too high around the planet to generate a clearly visible cavity in the disk.
This is a one more proof that a planet really close to the central star is unlikely responsible of the observed properties of the system (Section 4.2.3).

So this type of analysis seems to exclude some type of planetary companions that would modify or destroy the spiral arm structure generated by the external star: these are planets too close to the central star (≤ 10 AU), or too massive ($\geq 7\ M_J$). Instead, the eccentricity of the planet orbit seems not to play a crucial role regarding the variability of the spirals.

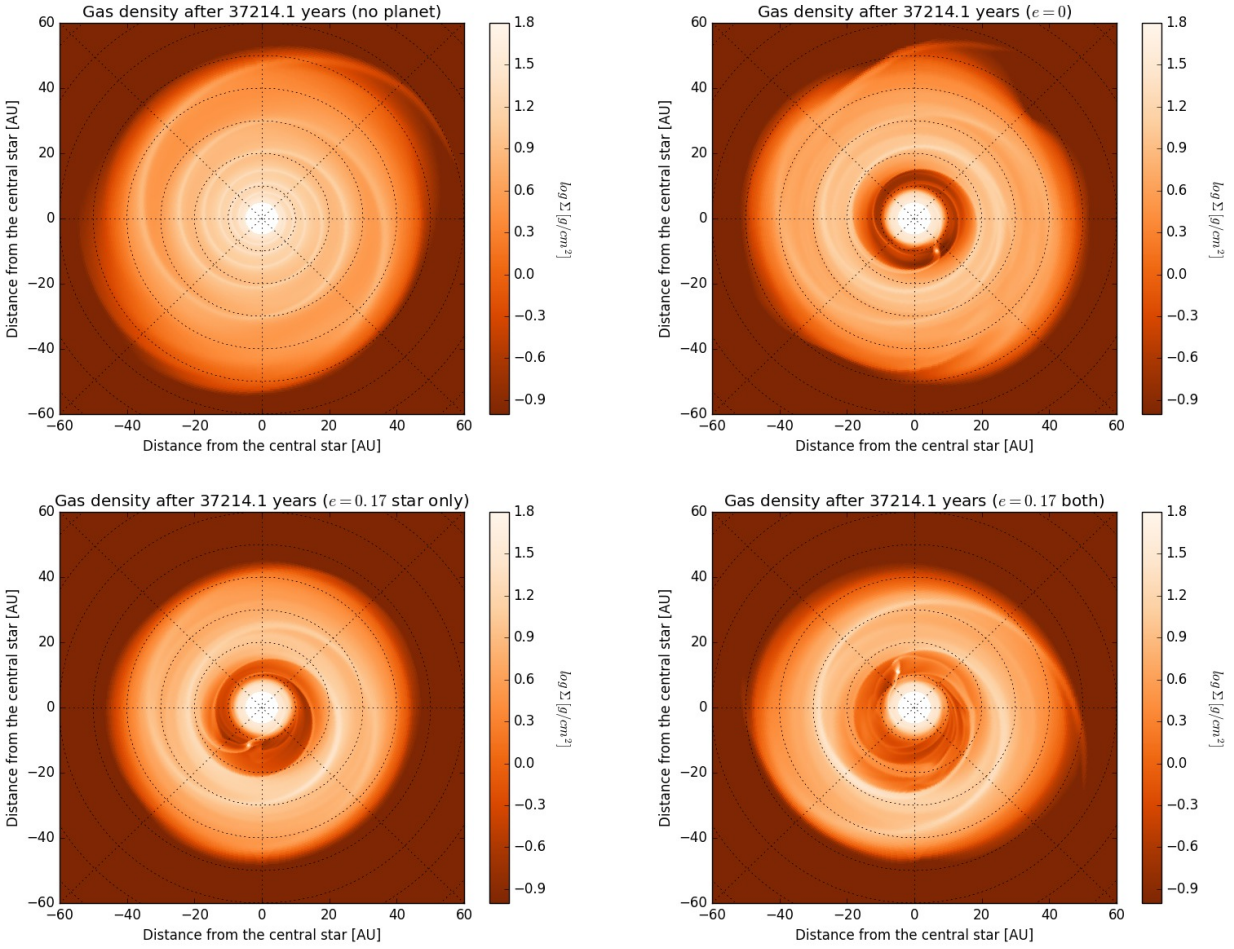

Figure 4.12: Final outputs for simulations with a 0.2 $M_\odot$ companion star mass. All the planets have a mass of 5 M_J and are initially positioned at 12 AU, with the three different eccentricities cases, specified in the title.

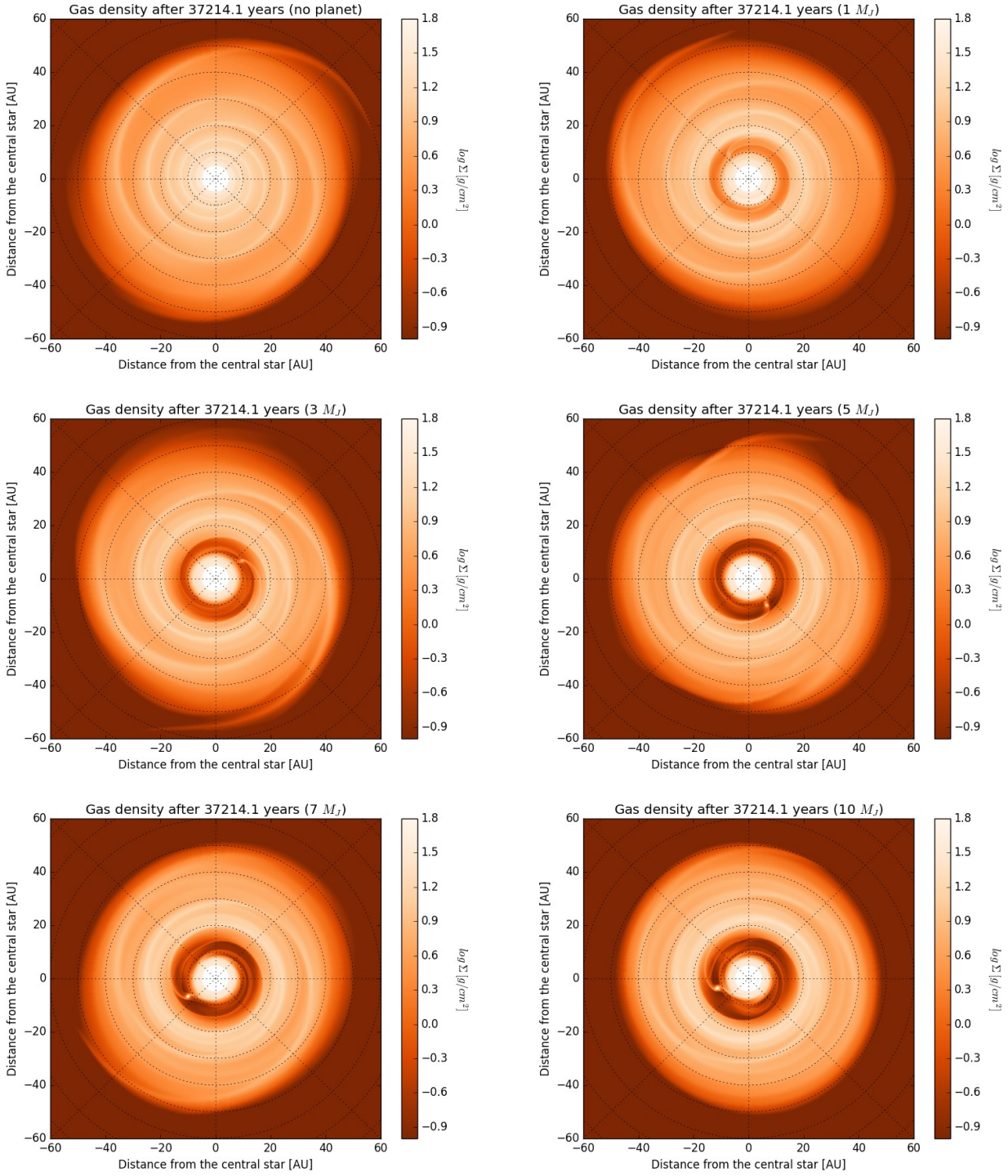

Figure 4.13: Final outputs for simulations with a 0.3 $M_\odot$ companion star mass. All the planets are initialized at 12 AU and both the companion orbits have $e = 0$. The mass is specified for each image.

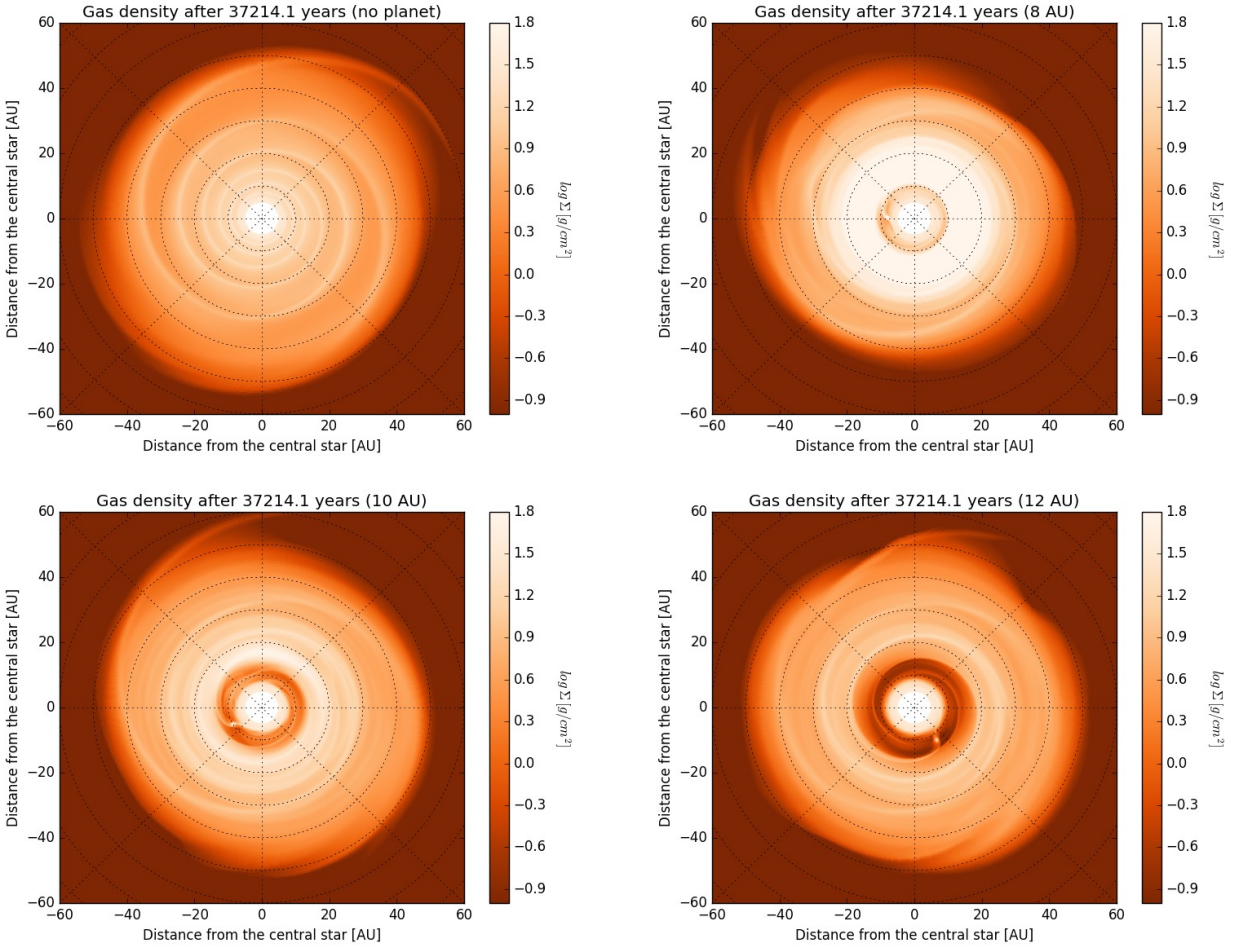

Figure 4.14: Final outputs for simulations with a 0.3 $M_{\odot}$ companion star mass. All the planets are of 5 M_J and both the companion orbits have $e = 0$. The distance at which they are initialized is specified for each image.

Chapter 5

Conclusions and future perspectives

5.1 Main purposes and simulation sets

The aim of this thesis work was the reproduction of some of the features that characterize the disk around the main star of the HD100453 system:

- the **double spiral arm pattern**: it is assumed to be due to the presence of a dwarf companion star, HD100453 B, positioned at a distance of 120 AU from the main object. Depending on the simulation, the companion star could have a mass of 0.2 $M_\odot$ or 0.3 $M_\odot$, and an eccentricity e that could be zero (circular orbit) or equal to 0.17, according to Wagner et al. (2018);

- the **truncation radius** R_T of the circumstellar disk around the main star: in such a configuration, according to the analytical models proposed by Artymowicz and Lubow (1994), a disk would be truncated at a radius equal to ~ 0.4 times the distance of the companion star (Section 1.6) for a circular orbit, and ~ 0.25 for an eccentric one (with $\mu = 0.15$ and $\alpha = 10^{-4}$). Two different initial conditions for the surface density has been applied, one with a cut-off radius R_C at 45 AU, and another one at 100 AU (Section 4.1.2), to see any difference that could depend on the disk mass in the external zone of the disk.

- the **inner cavity**, which extend from the central star to $\sim$ 16 AU (Benisty et al., 2016): its formation is attributed to the cleaning process that typically follows the formation of a planet in a disk (Paardekooper and Mellema, 2004). So, together with the dwarf star, a second planetary companion has been added. The set of simulations performed placed this planet at 8, 10, 12 and 15 AU, with a mass that could be 1, 3, 5, 7 or 10 M_J. Moreover, it has been simulated with an initial eccentricity equal to 0, or even to 0.17, if also the dwarf star orbit was eccentric.

All the simulations were run for a time equal to 40 periods of the 0.3 $M_\odot$ companion star, without the planet, that corresponds to about $3.7 \cdot 10^4$ years.

They have been performed in a 2-dimensional frame, looking mostly at the evolution of the surface density $\Sigma(r, \varphi)$ of the gas. This needs to be considered while checking the obtained results, since the observed images are based on dust scattered light. Moreover, the disk is inclined of about 28° degrees (Wagner et al., 2018) with respect to the line of sight, and even this factor can influence some of the obtained results.

5.2 Simulation results

5.2.1 Disk truncation

As a first result of the simulations, the **truncation** of the circumstellar disk has been verified, almost immediately after a few orbits of the companion, so in a dynamical timescale. Looking at the density profiles, it's clear that after about $R_T = 40 - 45$ AU the surface density drops pretty rapidly, reaching the lowest values (between $10^{-3} - 10^{-4}\, g/cm^2$) beyond 50 AU just after about 2-3 orbits of the companion star. This happens for both the simulations with the cut-off radius (in the surface density initial condition) at 45 and 100 AU. The truncation radius for an eccentric orbit of the companion doesn't change; a difference regards the values of Σ, that are higher in the region beyond 50 AU, but still very low ($< 10^{-2}\, g/cm^2$).

Making a comparison with the analytical models by Artymowicz and Lubow (1994), it seems that the simulations provided values for R_T in a mid way between the ones predicted for a circular orbit of the companion ($R_T \sim 50 - 55$ AU) and an eccentric one ($R_T \sim 30$ AU). However, the estimate from the simulations is just qualitative; while the analytical models obtained it as the radius where the tidal resonances (due to the gravitational perturbations from the companion star) equal the viscous stresses that characterize the gas. So, a slight difference is plausible.

5.2.2 Spiral arms

Like the disk truncation, even the double spiral arm pattern is visible just after a few orbits of the companion star. A bridge-like structure appears immediately at the beginning of the simulations, and it transfers the gas around the dwarf. It breaks after 5-6 orbits when $e = 0$, leaving the arm that points towards the companion. For an eccentric orbit this structure can last until 15-20 orbits, even if it's present only for a short time after the periastron.

Let's have a look on the similarities and the differences between simulated and observed arms:

- they appear even in the inner regions of the mesh, but their presence there isn't realistic because of the inner cavity.
- They develop in clockwise direction, contrary to the companion orbit, but they have its rotational period.
- Their separation is of about 180°, in agreement with the observations.

- The luminosity of the SW arm (the one pointing the companion) is higher than the luminosity of the other one, both in simulations and in observations.

- Their extension from simulations results similar and equal to about 50 AU, after reaching a stable configuration after about 10 orbits. This is in agreement only with the NE arm, the SW results extended until 39 AU in the observations. This is probably due to projection effects, since the disk is inclined of $\sim 28°$ with the SW region being the nearest one.

- the simulated spirals are much more wrapped than the observed ones. This can be seen through the pitch angle values, that results of less than 7° in the simulations, and between 30° and 38° in the observations. This difference can be generated both by projection effects and by a different distribution of the dust in the surface of the spirals with respect to the gas, which is integrated along the vertical axis in the simulations.

To find the pitch angles, the spirals have been fitted with a *logarithmic spiral*, with equation $r = a\, e^{b\varphi}$.

The spirals results to be quite stable when the companion star has a circular orbit. But when $e > 0$, their appearance strictly depends on the dwarf star position: they almost disappear after about 0.2 orbits after the apoastron and they appear stronger than the previous case after about 0.2 orbits after the periastron. For this reason, when the star orbit is eccentric, the spirals have been modeled only in this configuration.
The luminosity seems to be more similar for the two spiral, but their extension and pitch angles are quite similar to the case with $e = 0$.

5.2.3 Planet characterization

With the hypothesis that the only responsible for the formation of the observed inner cavity is a planetary companion inside it, let's summarize what has been done to characterize it.
The main ways to do that involve the wideness of the cavity that it generates with time, and the effects that it has on the double spiral arm pattern generated by the external companion star:

- the cavity has an outer border of ~ 16 AU (Benisty et al., 2016), and an inner border lower than the R_{inf} value due to the Stockholm condition (Section 3.4.2). Planets that are initialized at a distance lower than 10 AU can't generate such a wide cavity, independently on their mass, and can be excluded as possible candidates. Also planets farther than 12 AU aren't good candidates, since the external border of the cavity appears much farther than 16 AU (Section 4.2.3). Moreover, planets of 1 M_J can't clean alone a very large zone in the disk, so they must be excluded since the inner border of the cavity is greater than R_{inf}.

- looking at the effects on the spiral arms, it can be possible to exclude very heavy planets, with $M_P \geq 7\,M_J$, since they cause a greater envelopment of the spirals, almost blending them with the main ring structure. The eccentricity of the planet seems not to be so decisive in modifying the structure of the spirals.

Looking at these two combined effects, it is possible to establish that, if a single planet is responsible for the formation on the cavity observed in the HD100453 system, this would be characterized by a mass between 3 and 7 M_J, and by a distance from the main star between 10 and 12 AU.

These results are obtained under certain assumptions: a single planet configuration is plausible, but not the only possible in this system; a cavity like the one observed can be created by the combined effect of more lighter planets inside it, but no simulations were run with this configuration during this thesis work.
Finally it must be considered that the wideness of the cavity considered, so the value of R_H, is inferred from dust light scattered maps (Figure 2.1 from Benisty et al. (2016)), that aren't forced to coincide with the gas distribution inside the disk. This may lead to some variations about the parameters that characterize the planet in the system.

5.3 Future perspectives

In this thesis work, the main mechanisms that can generate some of the main features of the HD100453 disk were confirmed, but their characteristics don't always coincide with observations (for example, the spirals appear much more wrapped in the simulations).
Immediate future improvements of this kind of work, needed to try to adjust or explain these inconsistencies, are:

- the extension to a 3-dimensional frame, always using the FARGO3D code. This would lead to visualize the system with the same inclination we observe ($\sim 28°$), and to understand the magnitude of the consequent projection effects, especially on the pitch angle of the spiral arms.

- Using a radiative transfer calculation code (like RADMC-3D (Dullemond, 2010)) it would be possible to simulate an image of the disk of HD100453, analyzing its emission due to dust. This could be compared with the results obtained with the previous simulations, that involve only the gas. The comparison would be useful in checking the validity of the physical processes here assumed, and eventually to correct them or improve other ones.

Moreover, other possible future developments could be the following:

- add a tiny disk of dust in the very inner region of the system. This disk, thanks to its high inclination with respect to the rest of the disk, would be the responsible for the creation of the **shadows** observed in the disk. Since their

location almost coincides with the origin of the spirals (Section 2.2.2), they can have an influence in modifying the shape or the extension of the spirals, but this is still unclear.

- Regarding the internal cavity, it could be done a study on how much the **photoevaporation** from the main star could contribute on its formation. A combination of planet formation and photoevaporation processes could be a reasonable hypothesis, since the system is really old ($\sim$ 10 Myr).

- Running the simulations for longer time, corresponding to more orbits of the companion(s). The running time applied was of about $4 \cdot 10^4$ years, but the system has an estimated lifetime of $\sim 10^7$ years. All the predicted structures can form in the short time interval performed, and seems even to be stable in time. But there's the possibility for long-term effects to get relevant and modify these structures.

- Application to other systems which show similar features, especially regarding the double spiral arm pattern and the disk truncation, where a dwarf external star hasn't (still) being detected (Section 2.3). It would be a method to see how massive a companion must be to generate the spirals, but not massive enough to be revealed.

Bibliography

ALMA
2015. First results from high angular resolution alma observations toward the hl tau region. *The Astrophysical Journal*, 808:L3.

Andrews, S. M., D. Wilner, A. Hughes, C. Qi, and C. Dullemond
2009. Protoplanetary disk structures in ophiuchus. *The Astrophysical Journal*, 700(2):1502.

Ansdell, M., J. Williams, L. Trapman, et al.
2018. Alma survey of lupus protoplanetary disks. ii. gas disk radii. *The Astrophysical Journal*, 859(1):21.

Armitage, P. J.
2011. Dynamics of protoplanetary disks. *Annual Review of Astronomy and Astrophysics*, 49.

Artymowicz, P. and S. H. Lubow
1994. Dynamics of binary-disk interaction. 1: Resonances and disk gap sizes. *The Astrophysical Journal*, 421:651–667.

Avenhaus, H., S. P. Quanz, H. M. Schmid, et al.
2014. Structures in the protoplanetary disk of hd142527 seen in polarized scattered light. *The Astrophysical Journal*, 781(2):87.

Balbus, S. A.
2003. Enhanced angular momentum transport in accretion disks. *Annual Review of Astronomy and Astrophysics*, 41(1):555–597.

Benisty, M., T. Stolker, A. Pohl, et al.
2016. Shadows and spirals in the protoplanetary disk hd 100453. *Astronomy and Astrophysics*, 597:A42.

Benítez-Llambay, P. and F. S. Masset
2016. Fargo3d: A new gpu-oriented mhd code. *The Astrophysical Journal Supplement Series*, 223(1):11.

Brauer, F., T. Henning, and C. Dullemond
2008. Planetesimal formation near the snow line in mri-driven turbulent protoplanetary disks. *Astronomy & Astrophysics*, 487(1):L1–L4.

Brogan, C., L. Pérez, T. Hunter, et al.
2015. The 2014 alma long baseline campaign: first results from high angular resolution observations toward the hl tau region. *The Astrophysical Journal Letters*, 808(1):L3.

Clarke, C., A. Gendrin, and M. Sotomayor
2001. The dispersal of circumstellar discs: the role of the ultraviolet switch. *Monthly Notices of the Royal Astronomical Society*, 328(2):485–491.

Collins, K. A., C. A. Grady, K. Hamaguchi, et al.
2009. Hd 100453: A link between gas-rich protoplanetary disks and gas-poor debris disks. *The Astrophysical Journal*, 697:557–572.

Dominik, C. and C. Dullemond
2008. Coagulation of small grains in disks: the influence of residual infall and initial small-grain content. *Astronomy & Astrophysics*, 491(3):663–670.

Dong, R., Z. Zhu, J. Fung, R. Rafikov, E. Chiang, and K. Wagner
2015a. An m dwarf companion and its induced spiral arms in the hd 100453 protoplanetary disk. *The Astrophysical Journal*, 816:L12.

Dong, R., Z. Zhu, and B. Whitney
2015b. Observational signatures of planets in protoplanetary disks. i. gaps opened by single and multiple young planets in disks. *The Astrophysical Journal*, 809(1):93.

Dullemond, C. P.
2010. http://www.ita.uni-heidelberg.de/ dullemond/software/radmc-3d/.

Gorti, U. and D. Hollenbach
2008. Photoevaporation of circumstellar disks by far-ultraviolet, extreme-ultraviolet and x-ray radiation from the central star. *The Astrophysical Journal*, 690(2):1539.

Hayashi, C.
1981. Structure of the solar nebula, growth and decay of magnetic fields and effects of magnetic and turbulent viscosities on the nebula. *Progress of Theoretical Physics Supplement*, 70:35–53.

Hughes, A. M., D. J. Wilner, C. Qi, and M. R. Hogerheijde
2008. Gas and dust emission at the outer edge of protoplanetary disks. *The Astrophysical Journal*, 678:1119–1126.

Klahr, H. H. and P. Bodenheimer
2003. Turbulence in accretion disks: vorticity generation and angular momentum transport via the global baroclinic instability. *The Astrophysical Journal*, 582(2):869.

Liffman, K.
2003. The gravitational radius of an irradiated disk. *Publications of the Astronomical Society of Australia*, 20(4):337–339.

Lin, D. and J. Papaloizou
1986. On the tidal interaction between protoplanets and the protoplanetary disk. iii-orbital migration of protoplanets. *The Astrophysical Journal*, 309:846–857.

Luhman, K., P. Allen, C. Espaillat, L. Hartmann, and N. Calvet
2009. The disk population of the taurus star-forming region. *The Astrophysical Journal Supplement Series*, 186(1):111.

Mamajek, E. E., M. R. Meyer, and J. Liebert
2002. Post-t tauri stars in the nearest ob association. *The Astronomical Journal*, 124:1670–1694.

Manara, C., D. Fedele, G. Herczeg, and P. Teixeira
2016. X-shooter study of accretion in chamaeleon i. *Astronomy & Astrophysics*, 585:A136.

Montesinos, M. and N. Cuello
2018. Planetary-like spirals caused by moving shadows in transition discs. *Monthly Notices of the Royal Astronomical Society*, P. L3.

Montesinos, M., S. Perez, S. Casassus, S. Marino, J. Cuadra, and V. Christiaens
2016. Spiral waves triggered by shadows in transition disks. *The Astrophysical Journal Letters*, 823(1):L8.

Paardekooper, S.-J. and G. Mellema
2004. Planets opening dust gaps in gas disks. *Astronomy & Astrophysics*, 425(1):L9–L12.

Paczynski, B. and B. Rudak
1980. Inner accretion disk in a close binary. *Acta Astronomica*, 30:237–247.

Papaloizou, J. and J. Pringle
1977. Tidal torques on accretion discs in close binary systems. *Monthly Notices of the Royal Astronomical Society*, 181(3):441–454.

Pringle, J.
1981. Accretion discs in astrophysics. *Annual review of astronomy and astrophysics*, 19(1):137–160.

Schütz, O., G. Meeus, and M. F. Sterzik
2005. Mid-ir observations of circumstellar disks. i. pre-main sequence objects. 431.

Shakura, N. I. and R. A. Sunyaev
1973. Black holes in binary systems. observational appearance. *Astronomy and Astrophysics*, 24:337–355.

Stoll, M. H. and W. Kley
2014. Vertical shear instability in accretion disc models with radiation transport. *Astronomy & Astrophysics*, 572:A77.

Stone, J. M. and M. L. Norman
1992. Zeus-2d: A radiation magnetohydrodynamics code for astrophysical flows in two space dimensions. i-the hydrodynamic algorithms and tests. *The Astrophysical Journal Supplement Series*, 80:753–790.

Strom, K. M., S. E. Strom, S. Edwards, S. Cabrit, and M. F. Skrutskie
1989. Circumstellar material associated with solar-type pre-main-sequence stars-a possible constraint on the timescale for planet building. *The Astronomical Journal*, 97:1451–1470.

Toomre, A.
1964. On the gravitational stability of a disk of stars. *The Astrophysical Journal*, 139:1217–1238.

Turner, N. J., S. Fromang, C. Gammie, et al.
2014. Transport and accretion in planet-forming disks. *Protostars and Planets VI*, Pp. 411–432.

Val-Borro, M. D., R. G. Edgar, P. Artymowicz, et al.
2006. A comparative study of disc-planet interaction. *Monthly Notices of the Royal Astronomical Society*, 370:529–558.

Wagner, K., D. Apai, M. Kasper, and M. Robberto
2015. Discovery of a two-armed spiral structure in the gapped disk in hd 100453.

Wagner, K., R. Dong, P. Sheehan, et al.
2018. The orbit of the companion to hd 100453a: Binary-driven spiral arms in a protoplanetary disk. *The Astrophysical Journal*, 854:130.

Waters, T. R. and D. Proga
2012. Parker winds revisited: an extension to disc winds. *Monthly Notices of the Royal Astronomical Society*, 426(3):2239–2265.

Weidenschilling, S.
1977. The distribution of mass in the planetary system and solar nebula. *Astrophysics and Space Science*, 51(1):153–158.

Wolk, S. J. and F. M. Walter
1996. A search for protoplanetary disks around naked t tauri stars. *The Astronomical Journal*, 111:2066.

Zhu, Z., R. P. Nelson, L. Hartmann, C. Espaillat, and N. Calvet
2011. Transitional and pre-transitional disks: Gap opening by multiple planets? *The Astrophysical Journal*, 729(1):47.